SANDIA REPORT
SAND2000-3082
Unlimited Release
Printed December 2000

Dispersive Velocity Measurements in Heterogeneous Materials

Wayne M. Trott, Jaime N. Castaneda, John J. O'Hare, Melvin R. Baer,
Lalit C. Chhabildas, Marcus D. Knudson, Jean-Paul Davis, and James R. Asay

Prepared by
Sandia National Laboratories
Albuquerque, New Mexico 87185 and Livermore, California 94550

Sandia is a multiprogram laboratory operated by Sandia Corporation,
a Lockheed Martin Company, for the United States Department of
Energy under Contract DE-AC04-94AL85000.

Sandia National Laboratories

Issued by Sandia National Laboratories, operated for the United States Department of Energy by Sandia Corporation.

Available to DOE and DOE contractors from
Office of Scientific and Technical Information
P.O. Box 62
Oak Ridge, TN 37831

Prices available from (703) 605-6000
Web site: http://www.ntis.gov/ordering.htm

Available to the public from
National Technical Information Service
U.S. Department of Commerce
5285 Port Royal Rd
Springfield, VA 22161

NTIS price codes
Printed copy: A04
Microfiche copy: A01

SAND2000-3082
Unlimited Release
Printed December 2000

DISPERSIVE VELOCITY MEASUREMENTS IN HETEROGENEOUS MATERIALS

Wayne M. Trott, Jaime N. Castañeda, John J. O'Hare
Thermal/Fluid Experimental Sciences Department

Melvin R. Baer
Engineering Sciences Center

Lalit C. Chhabildas, Marcus D. Knudson, Jean-Paul Davis and James R. Asay
Weapons Science Applications Department

Sandia National Laboratories
P.O. Box 5800
Albuquerque, New Mexico 87185-0834

Abstract

In order to provide real-time data for validation of three dimensional numerical simulations of heterogeneous materials subjected to impact loading, an optically recording velocity interferometer system (ORVIS) has been adapted to a line-imaging instrument capable of generating precise mesoscopic scale measurements of spatially resolved velocity variations during dynamic deformation. Combining independently variable target magnification and interferometer fringe spacing, this instrument can probe a velocity field along line segments up to 15 mm in length. In high magnification operation, spatial resolution better than 10 μm can be achieved. For events appropriate to short recording times, streak camera recording can provide temporal resolution better than 0.2 ns. A robust method for extracting spatially resolved velocity-time profiles from streak camera image data has been developed and incorporated into a computer program that utilizes a standard VISAR analysis platform. The use of line-imaging ORVIS to obtain measurements of the mesoscopic scale dynamic response of shocked samples has been demonstrated on several different classes of heterogeneous materials. Studies have focused on pressed, granular sugar as a simulant material for the widely used explosive HMX. For low-density (65 percent theoretical maximum density) pressings of sugar, material response has been investigated as a function of both impact velocity and changes in particle size distribution. The experimental results provide a consistent picture of the dispersive nature of the wave transmitted through these samples and reveal both transverse and longitudinal wave structures on mesoscopic scales. This observed behavior is consistent with the highly structured mesoscopic response predicted by 3-D simulations. Preliminary line-imaging ORVIS measurements on HMX as well as other heterogeneous materials such as foam and glass-reinforced polyester are also discussed.

Acknowledgments

The authors thank Lloyd Bonzon and operations personnel at the Sandia Explosive Components Facility gas gun for their help and cooperation in the execution of the experiments described here. In particular, the excellent technical assistance of Heidi Anderson, John Liwski, Michael Navarro and Daniel Sanchez is gratefully acknowledged. We also thank William Reinhart and Tom Thornhill for much valuable assistance in target fabrication and the execution of point VISAR measurements. In addition, we are very grateful to Dr. Stephen A. Sheffield (Los Alamos National Laboratory) for many helpful comments and suggestions on this work and for his generous assistance in the preparation of our HMX gas gun target fixtures. Moreover, we wish to thank Dr. D. P. Dandekar (U.S. Army Research Laboratory) for his technical insight and help in supplying samples for our experiments on Z-cut sapphire. We also thank Dr. Mike Boteler (U.S. Army Research Laboratory) for supplying samples for our experiments on glass-reinforced polyester.

Preface

This work was supported by Laboratory Directed Research and Development (LDRD) funding. The Appendix lists reporting information required by that funding source.

Contents

Figures

Figures (continued)

I. INTRODUCTION

Microscopic material descriptions such as grain morphology, internal defects, tensile strength, shear behavior, heat conduction, etc. in large part drive the detailed response of a heterogeneous material (e.g., a pressed granular explosive) to impact loading. Analysis of this detailed response is addressed by the current capabilities for three-dimensional (3-D) numerical simulations. [1] These calculations explore the correlation between microscopic properties and the response of the material at mesoscopic scales, including detailed spatial variations in stress and thermal fields (dispersive behavior). To support the computational efforts, there is a critical need for diagnostic development that can effectively probe the material response at the requisite mesoscopic scale. Characteristic length scales can actually vary from a few μm (e.g., for PZT materials) to a few mm (e.g., for concrete).

Velocity interferometry is a well-established and frequently utilized technique for determining the velocity-time behavior of many types of samples. In numerous applications time-resolved data from different interferometer designs (such as VISAR, ORVIS, and Fabry-Perot) have led to improved understanding of physical and chemical processes associated with high-rate deformation. The most commonly employed approach involves "single point" measurements wherein an average velocity is measured (as a function of time) over a probe laser spot typically ranging from 50-200μm in diameter. In this configuration, neither macroscopic scale spatial variations in the response of sample regions larger than the spot size nor small-scale variations within this diameter can be determined.

The wealth of information potentially available in spatially resolved measurements provides a compelling motivation to develop more sophisticated approaches to velocity interferometry. In 1986 Gidon and Behar [2] reported a Fabry-Perot design that captured the velocity-field of an entire surface at a single time. Subsequent developments included line-imaging Fabry-Perot and VISAR interferometers [3,4] for continuous measurement of the velocity of a line segment on a moving surface, and an extended full-field Fabry-Perot method [5] for determining velocity as a function of both position and time (using a framing camera to record the data in a time sequence). An important recent enhancement of conventional "single point" VISAR methods is the development of a multi-point system, featuring simultaneous velocity-time measurements at up to seven different locations on the target sample. [6]

In 1995 Baumung et al. [7] described a simplified design for a high-resolution, line-imaging interferometer with modest requirements for the continuous wave laser source (~1 W). We have utilized similar approaches in adapting the conventional optically recording velocity interferometer system (ORVIS) configuration [8,9] to fine-scale, spatially resolved measurements. This capability of line-imaging ORVIS has been evaluated in laser-driven flyer studies and extensively applied to well-controlled, well-characterized impact loading experiments at the Sandia National Laboratories Explosive Components Facility gas gun. Initial tests exploring the mesoscopic scale dynamic response of a variety of heterogeneous materials have been discussed elsewhere. [10-12]

In this report we provide a summary of our efforts over the last three years to develop line-imaging ORVIS as a high-resolution diagnostic for investigation of the detailed response of heterogeneous materials to impact loading. In Section II we briefly describe essential elements of the current line-imaging ORVIS optical design along with a complementary technique for simultaneous measurement of an areal (2-D) velocity map at one point in time. Methods for line-imaging ORVIS data reduction are discussed in Section III. The primary analysis tool is an image analysis program that generates spatially resolved velocity-time records by adapting widely utilized "push-pull" VISAR analysis methods. [13] Some advantages and limitations of Fast Fourier Transform (FFT) filtering of the ORVIS image data for this purpose are also presented. In Section IV we discuss results from initial system evaluation experiments. These preliminary tests on a system with known response (e.g., fused silica under symmetric impact conditions) provided useful information on detector characteristics and data analysis. Section V presents experimental results on the response of low-density pressings of granular sugar (inert simulant material for the explosive HMX) as a function of both impact velocity and changes in particle size distribution. These results demonstrate that transverse as well as longitudinal wave structures at the mesoscopic scale can be captured by the line-imaging ORVIS technique. The results compare favorably to the detailed material response predicted by computational modeling of the low-density sugar at the mesoscale. In Section VI we present preliminary data from tests on low-density pressings of HMX. These tests address the effects of chemical energy release on the spatially resolved velocity-time behavior. In Section VII we discuss the results of line-imaging ORVIS tests on a variety of other systems. These experiments illustrate the wide applicability of the ORVIS diagnostic. Finally, conclusions and recommendations for future work are presented in Section VIII.

II. EXPERIMENTAL DEVELOPMENTS

A. Line-Imaging ORVIS Methods

Techniques for generating a line-imaging ORVIS assembly are illustrated in Fig. 1. As in the conventional configuration, coherent light from the source laser is directed through a small hole in a turning mirror and then focused onto the target of interest. Diffusely reflected light from the target is collected and roughly collimated by the focusing lens (L1); the collimated beam reflects off the turning mirror and is reduced in diameter by the down-collimating telescope optics (L2, L3). A 50/50 beamsplitter splits the beam into two equal-intensity components, one of which serves as a reference leg. The second leg passes through a variable-length fused silica cylinder. This optical component imparts a time delay (proportional to the cylinder length) in the second beam. Observed motion of the interference fringes generated by beam recombination (with mirrors tilted so as to produce a "straight-line" pattern) is directly proportional to target velocity. This motion can be recorded by a high-speed streak camera (image rotation and relay optics may be utilized in this operation, depending on the desired location of the streak camera and the orientation of its entrance slit). The focusing/collection lens (L1) and telescope optics (L2, L3) can be adjusted to produce a magnified image of the target at the recombination plane (i.e., the location of best fringe contrast); in this mode, local

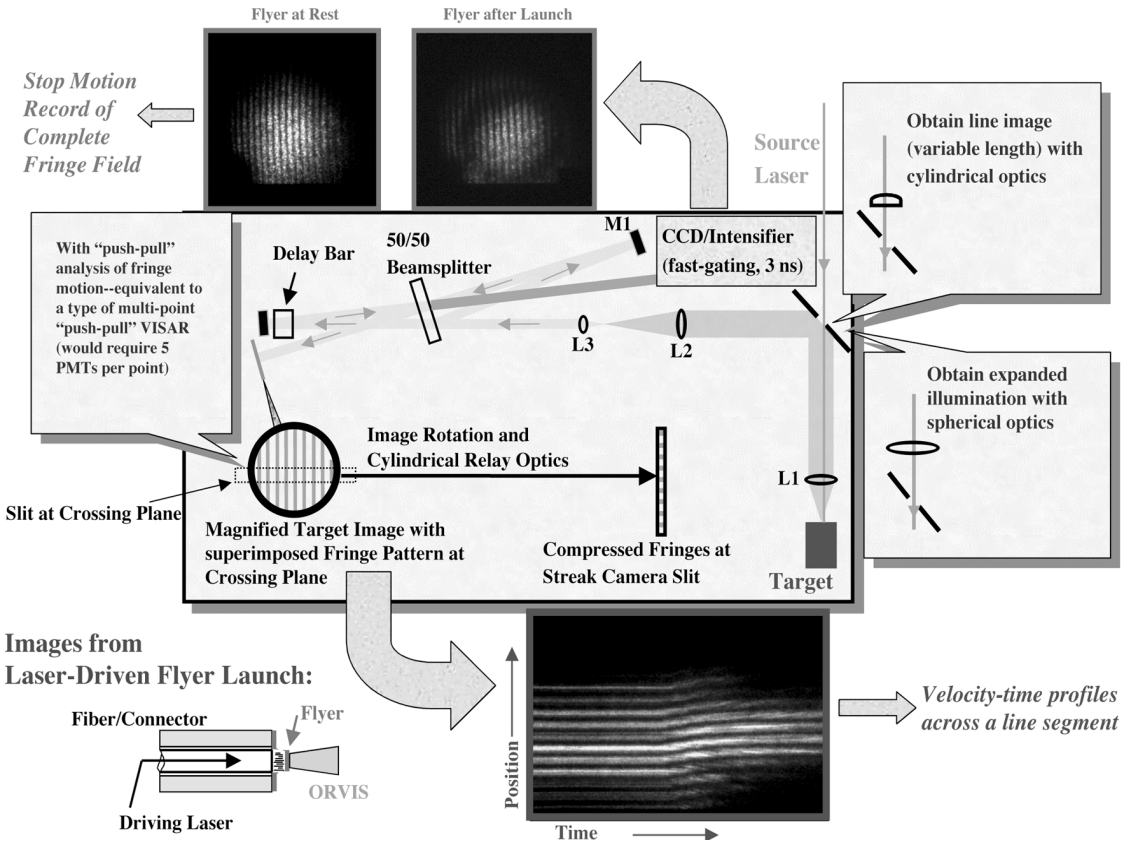

Figure 1. Schematic of experimental configuration for line-imaging ORVIS and simultaneous stop-motion imaging of full fringe field.

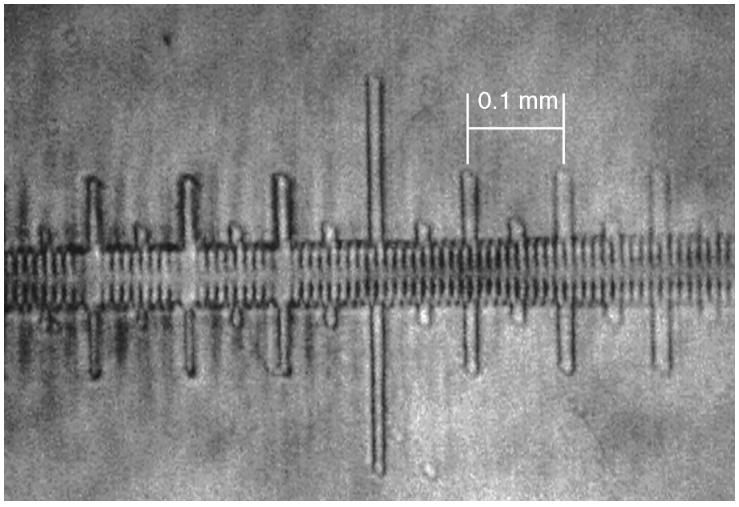

Figure 2. Image of reticle mounted at target plane (as viewed at recombination plane).

variations in target surface velocity are reflected in corresponding local translations of the superimposed fringe field. Facile control of both image size and spatial resolution can be achieved via suitable variations in the relative angles and spacing of the interferometer mirrors as well as the spacing and focal lengths of the imaging optics (see below).

The high-resolution imaging capability of the ORVIS optical configuration is illustrated in Fig. 2. To produce this image, a reticle was mounted in contact with a reflective surface at the focus of lens L1. A CCD camera then recorded the magnified image produced at the recombination plane by a particular combination of lenses L1, L2, and L3 (in order to view the image without fringes, light from one leg of the interferometer was blocked in this instance). The finest ruling on the reticle corresponds to a 10-μm separation at the target plane. This small separation is clearly resolved across the field of the recombination plane. By superimposing the reticle image on a calibrated scale mounted at this plane, the effective magnification of the instrument can be easily established. In a similar manner, the interferometer fringe spacing can be referenced to distances at the target plane. A typical image relating these quantities is shown in Fig. 3. Markings delineating 1-mm distances at the recombination plane are evident at the bottom. Comparison of the two scales indicates a target magnification of 18.5 in this case. The recorded fringe spacing corresponds to very nearly 50 μm at the target.

We have examined the effects of varying the diameters and focal lengths of the image producing optics (L1, L2, and L3), as well as the distances between these components. Image magnification can be adjusted over a wide range and simple scaling relations apply in many cases. Figure 4 illustrates simple scaling behavior in response to large changes in focal length for telescope elements L2 and L3, respectively. These results were obtained with a laboratory scale interferometer configuration (1.5-meter distance from L1 to L2, ~1-meter interferometer cavity length). Under these conditions, image magnification is very nearly a linear function of the focal length of L2 and the reciprocal of the focal length of L3, respectively. In any case, the image magnification can be easily calculated via standard combination lens formulas. Image magnification is generally relatively insensitive to target distance from the interferometer. We have operated line-imaging interferometers at distances up to 11 meters with negligible deterioration in image quality or intensity. As Fig. 4 suggests, the three-lens image producing optics tend to generate large magnification; however, a low magnification (< 2x) setup with good image quality and depth of field can be obtained by introducing two additional relay lenses between L1 and L2. As a result, the field of view can easily be extended to line segments up to 15 mm in length, depending on the detector geometry (streak camera photocathode diameter, etc.). Together with independently variable fringe spacing controlled by the angles and positions of the interferometer mirrors, the wide latitude in imaging parameters enables the study of materials with widely different characteristic scale lengths. These characteristics also permit location of the interferometer system at a safe, variable distance from an impact-loaded sample (e.g., located in a gas gun target chamber).

As demonstrated by Baumung et al., the target illumination can be confined to a thin line segment by placing a cylindrical lens of suitable focal length in the source laser path ahead of the turning mirror aperture. [7] Alternatively, one can place a spherical lens in

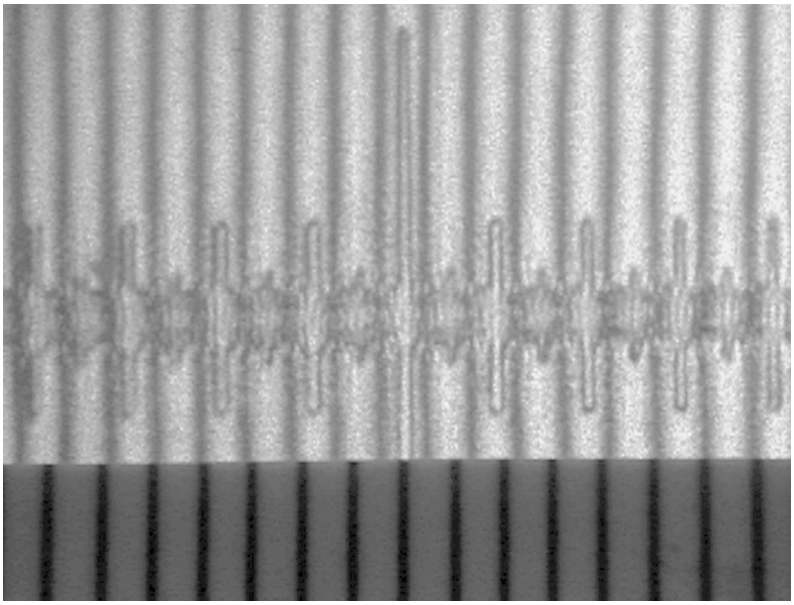

Figure 3. Interferometer fringes with magnified image of reticle; target magnification and fringe spacing can be determined from scale at bottom of image (1-mm divisions).

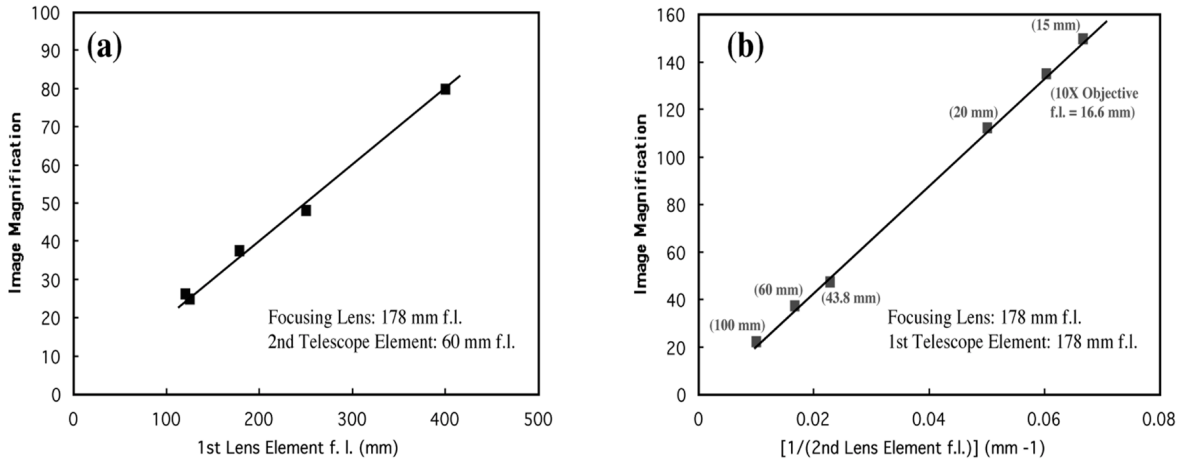

Figure 4. Effect of telescope element focal lengths on ORVIS interferometer image magnification. (a) Variation of focal length for L2; (b) Variation of focal length for L3.

this position and expand as desired the illumination area on target. A line image for recording by the streak camera can still be produced in this mode by placing a rectangular aperture of the desired width near the image/recombination plane. This approach requires a suitable combination of source laser power and target reflectivity to ensure sufficient signal at the streak camera; however, it enables a powerful complementary technique that utilizes a redundant recombined beam that propagates off the front side of the beamsplitter (cf. Fig. 1). In probing this beam, a fast-gating (<3 ns) intensifier/CCD can be used to capture a stop-motion image of the full fringe field at one point in time. In addition to producing data that can be reduced to generate a 2-D map of target surface velocity at one instant, this technique provides an informative diagnostic for the behavior of the line-imaging ORVIS fringe records (e.g., in locating regions of surface curvature that leads to vignetting of signal at the streak camera).

Recently, we have developed and tested several improvements to the ORVIS optical configuration described previously. A substantial enhancement in image quality was achieved by replacing the turning mirror containing the small hole (cf. Fig. 1) with a polarization-sensitive beamsplitter (CVI Laser, Inc.). This optical component was designed to transmit horizontally polarized laser light (Nd:YVO_4, 532 nm) at an efficiency of 80 percent and to reflect light at an efficiency of 42 percent, providing significantly higher overall efficiency than a simple 50/50 beamsplitter. Examples of on-axis image degradation obtained with the turning mirror are illustrated in Fig. 5. Various parameters such as system magnification, distance of the turning mirror from the interferometer, and characteristics of target reflectivity (e.g., relative intensity of specular and diffuse components of reflection) were found to influence the image quality (cf. Fig. 5b and Fig. 5e). Fig. 5c and 5d show that these deleterious effects were essentially eliminated with the beamsplitter in use.

An interesting and useful refinement of the approach to line illumination reported by Baumung et al. [7] involves the removal of L1 from the source laser beam path and relocation of this element to a position between the turning mirror (or beamsplitter) and L2. In this configuration, established techniques of laser light sheet generation [14] can be used to tailor independently the width and length of the illumination line segment on target. With this approach, the target illumination optics are completely decoupled from the collection optics in general and the focal length of L1, in particular. An additional advantage of this method is the elimination of source laser light (i.e., backreflected from L1) in the fringe signal reaching the streak camera.

The laser light sheet method utilizes a combination of one spherical and three cylindrical optics. A schematic diagram and photograph of the optical assembly that we have used is shown in Fig. 6. The spherical lens and the last cylindrical lens are positioned to transform the incoming collimated beam into a line of minimal width. This is accomplished by locating the cylindrical lens at twice its focal length from the target and the spherical lens at an additional distance equal to its focal length plus the target/cylindrical lens distance. By separating the optics in this manner, the cylindrical lens is used to image the small diameter of the focal spot of the first lens to the target in one dimension. The length of the line segment, on the other hand, is determined by the

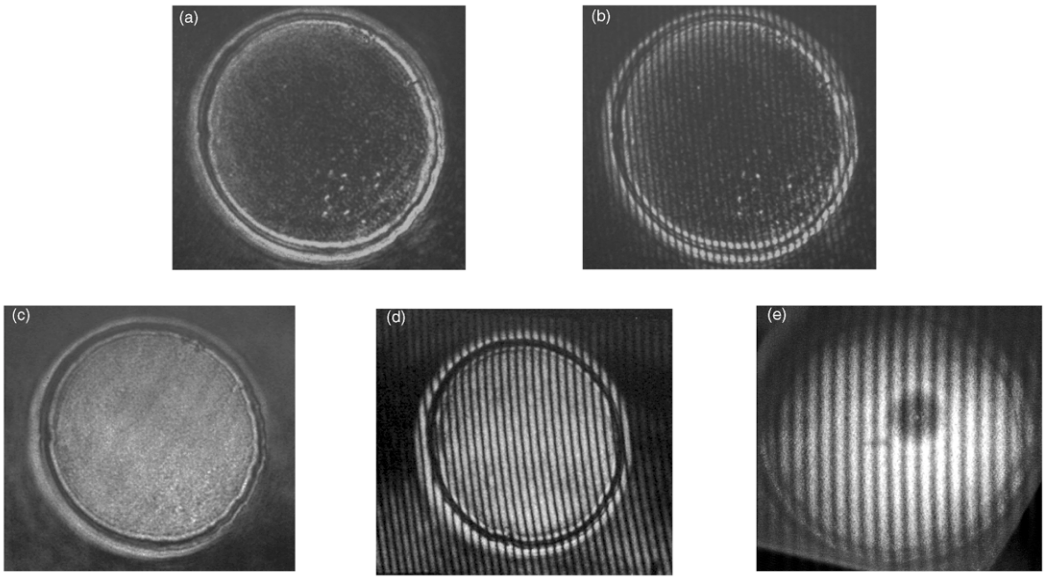

Figure 5. Magnified images of laser-driven flyer target (acquired at interferometer recombination plane). (a) central portion of image greatly attenuated in intensity using turning mirror with central hole; (b) attenuation also seen in fringes; (c) uniform illumination achieved with beamsplitter; (d) uniform fringe intensities obtained with beamsplitter; (e) smaller region of attenuation obtained with turning mirror in a different optical configuration.

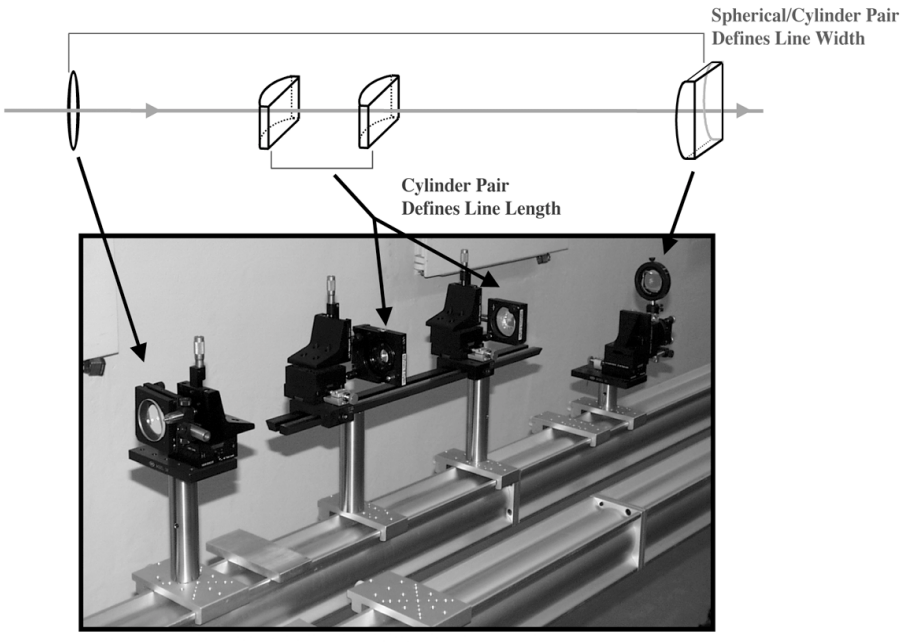

Figure 6. Schematic diagram and photograph of line illumination optical system

positions and focal lengths of the second and third cylindrical lenses in combination with the spherical lens. [14] With the position of the spherical lens fixed to provide the minimal line width, the second and third cylindrical lenses are moved (essentially in tandem) to vary the line length as desired. Very thin (<150 μm) line segments can be produced in this manner, as illustrated in Fig. 7. If the laser source can provide sufficient intensity for the experiment, nearly uniform illumination can be achieved over several mm in the horizontal dimension by using only the center portion of a relatively long line. Uniform illumination of a 480-μm-diameter, aluminum, laser-driven flyer target is shown in Fig. 8.

Isolation of the input and collection optics in the line-imaging ORVIS assembly provides additional flexibility in determination of the system magnification. In some target configurations, physical access to the interface to be measured is restricted (e.g., in a target requiring an interferometer window in contact with the interface). Hence, imaging a reticle positioned at the target plane may be difficult (at a minimum requiring the assembly of a "dummy" target containing the reticle). Under these conditions, a projection system can be used to provide a scale for reimaging at the recombination plane. For this purpose, a calibrated pinhole, slit or reticle is placed in the source laser path and a spherical lens is used to image the distance standard onto the target interface. The magnification of the image can be easily varied by adjusting the distances between the standard, spherical lens, and target according to simple lens formulas. Figure 9 provides two examples of this technique. Figure 9a shows an image (acquired at the recombination plane) of a reticle positioned at the target plane and illuminated by the image of a 300-μm diameter pinhole projected to the target at a magnification of x2. Direct projection of a reticle image (also at x2 magnification) onto a 480-μm-diameter flyer target is shown in Fig. 9b.

B. Laser-Driven Flyer Test Platform

Much of the initial evaluation of the line-imaging ORVIS and stop-motion fringe field imaging techniques, as well as the associated data reduction, has utilized a test platform for pulsed laser-driven flyer generation. The rapid (ns timescale) accelerations and fine-scale (<10 μm) spatial features (e.g., nonplanarity, growth of perturbations due to drive instabilities) observed in the laser launched flyers provide an excellent sampling testbed for assessing the capabilities of these diagnostic methods. The relevant details of the laser-driven flyer apparatus have been described previously. [15,16]

C. Line-Imaging ORVIS Assembly For Gas-Gun Experiments

A compact version of the line-imaging ORVIS has been assembled and tested at the Explosive Components Facility (ECF) gas gun at Sandia National Laboratories. This system combines the interferometer optics, laser source and streak camera/intensifier/CCD detector on a single 2’ x 6’ optical breadboard. Coupling of this diagnostic to the test samples required design and assembly of a complex optical interface that could accommodate the 11-meter path to the gas gun target chamber. For stability as well as facile substitution and alignment of imaging optics (e.g., to adjust

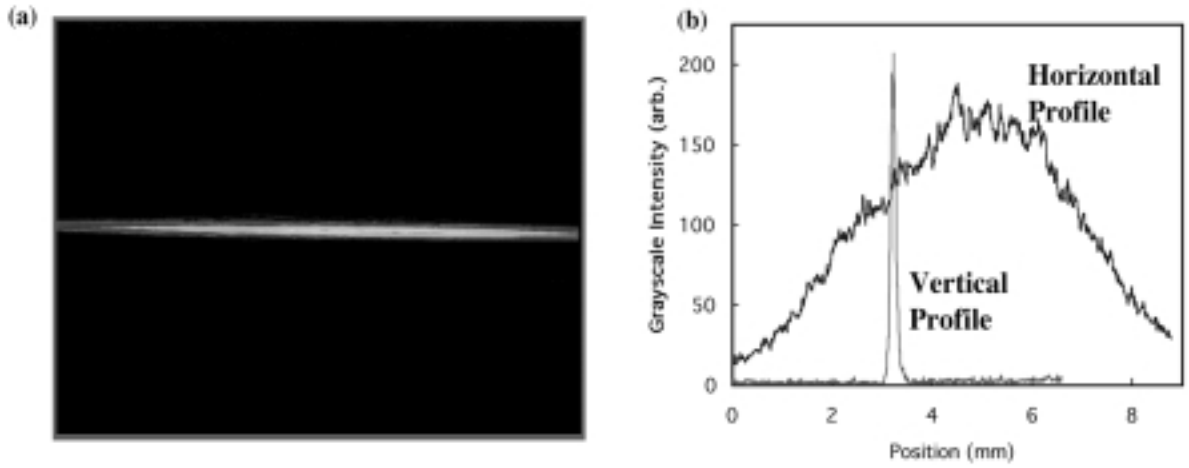

Figure 7. Beam profile data for line segment target illumination using laser light sheet optics: (a) CCD camera image of line illumination; (b) intensity profiles illustrating line width ~150 μm.

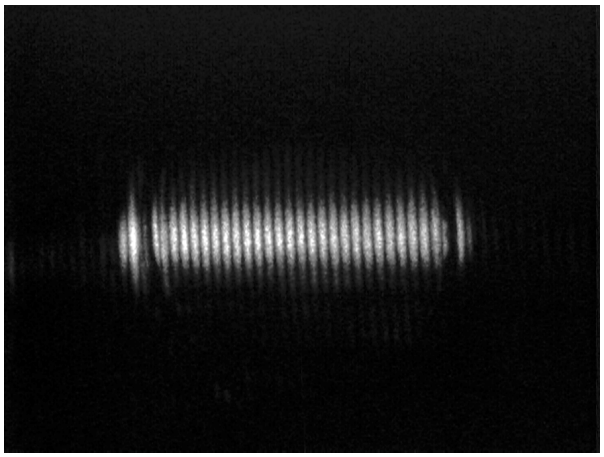

Figure 8. Uniform line illumination of 480-μm-diameter laser-driven flyer target.

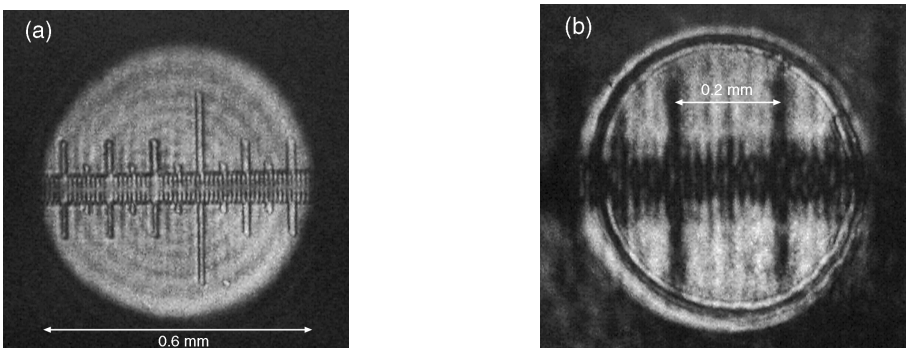

Figure 9. Images illustrating projection technique for determination of system magnification: (a) illuminated pinhole imaged onto target; (b) reticle imaged onto target.

image magnification in two different experiments), the input and collection legs of the system were mounted on separate long rails. This rail assembly is shown in Fig. 10. Gas-gun targets that allowed for simultaneous line-imaging ORVIS and standard dual-delay-leg, "push-pull" VISAR measurements on a variety of materials were designed and fabricated. Simultaneous use of both techniques permits direct comparison of spatially resolved vs. single spot ("continuum"-like) data. In most cases, the diagnostics were used to probe different regions of the sample; however, a few experiments incorporated a dichroic beamsplitter that enabled both simultaneous *and* spatially overlapped line-imaging ORVIS and point VISAR measurements. Specific target designs will be described in the sections devoted to experimental results from different materials (see below).

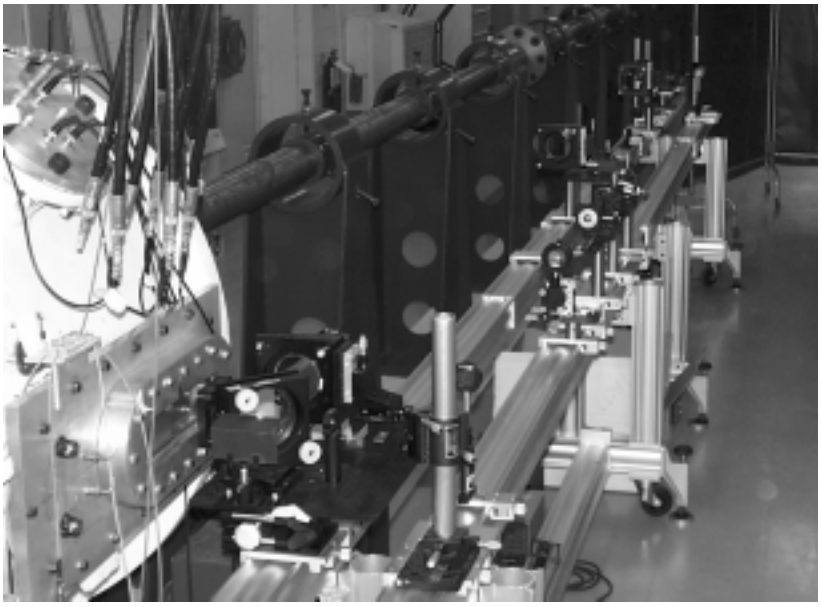

Figure 10. Rail system used to mount input and collection optics for line-imaging ORVIS assembly at gas gun facility; in this view, collection optics appear on left rail.

III. DATA REDUCTION METHODS

To exploit the information associated with each recorded fringe in line-imaging ORVIS data, it is necessary to develop a suitable method for image analysis. Baumung et al. [7] described an approach (analogous to reduction of VISAR interferograms) that extracts the intensity modulation data along lines parallel to the time axis of the streak camera record. The simplest implementation of this reduction method generates components that are, in effect, quadrature coded using intensity "lineouts" along the center of a fringe and at 1/4 the distance to the center of a neighboring fringe. This procedure is illustrated in Fig. 11. In this case, the image data captured the acceleration of a laser-driven flyer, as measured at the distal free surface. Velocity-time data can be obtained by importing the intensity records into standard VISAR data reduction software. Figure 12 provides a comparison of a single-line velocity-time record extracted in this manner with the velocity history obtained using a global treatment of the image data. [17]

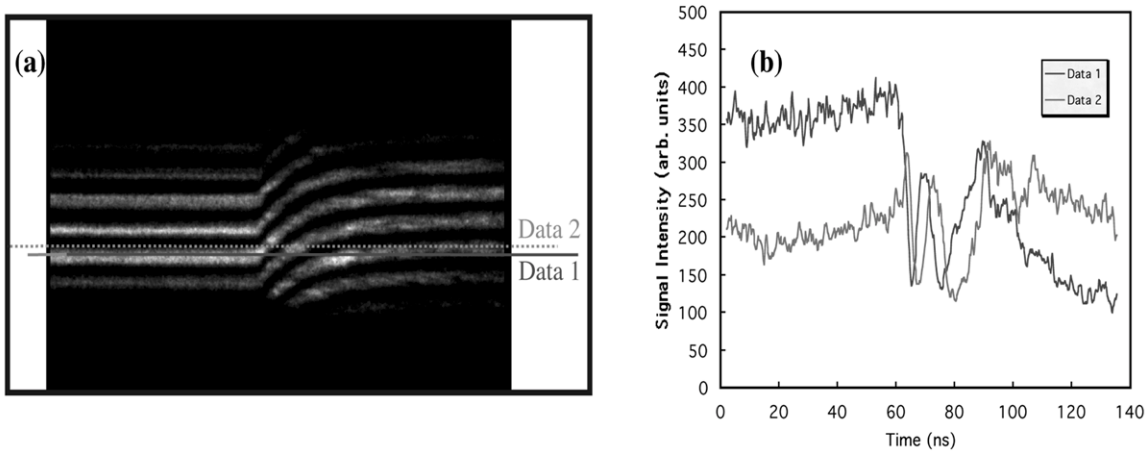

Figure 11. Method for extracting single fringe velocity-time data from line-imaging ORVIS record: (a) image data for laser-driven flyer launch; (b) intensity "lineouts" for input to VISAR analysis.

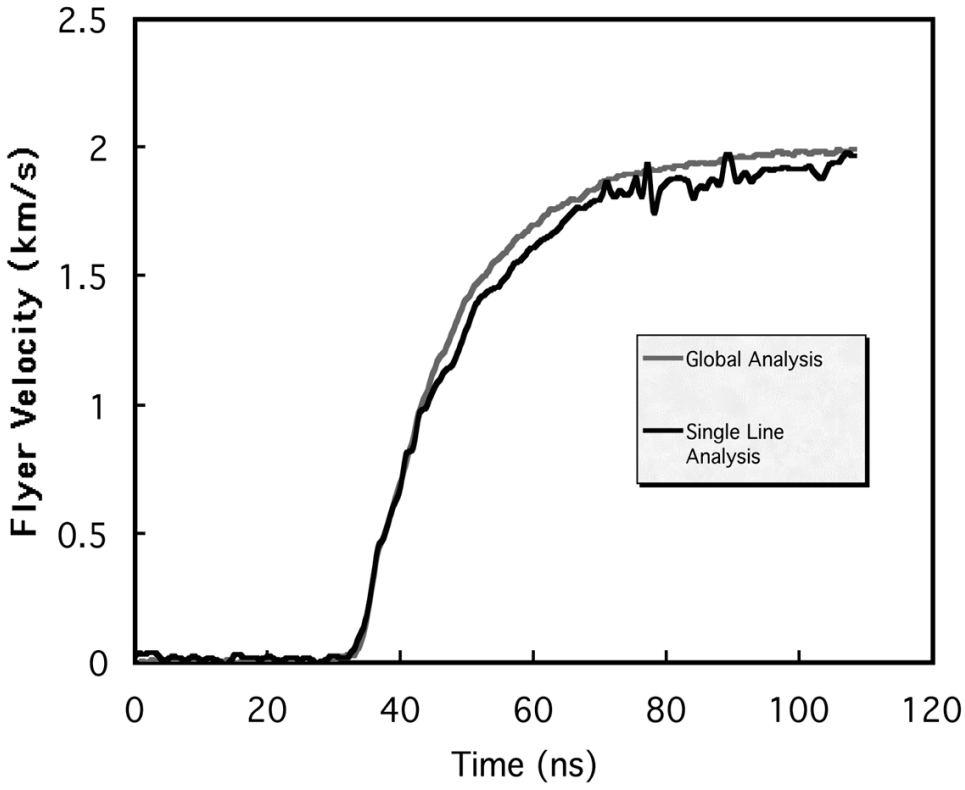

Figure 12. Comparison of results from single line data reduction vs. global data reduction method.

The plots demonstrate that fairly good agreement in the results of these reduction methods can be obtained. One clear drawback of this approach, however, is the requirement for an additional record that accurately tracks the reflected beam intensity (a necessary input to the VISAR analysis software). A reasonable method for approximating the reflected intensity consists of spatially averaging the intensity “lineout” data over a few fringe cycles. Unfortunately, in experiments involving fine-scale perturbations, significant intensity fluctuations (independent of fringe motion) can be encountered even within this restricted field of image data.

A more robust approach applies "push-pull" VISAR analysis concepts [13] to process the ORVIS fringe records. In this technique, "lineouts" are recorded at positions corresponding to the fringe center as well as at 1/4, 1/2, and 3/4 the distance to the center of a neighboring fringe. These data can be treated in the same manner as that recorded by four PMT channels in a "push-pull" VISAR. This approach is shown schematically in Fig. 13. In examination of numerous fringe records from flyer data, the results are uniformly consistent with averaged results from the global reduction program [17] and we have encountered very few difficulties (e.g., spurious fringe jumps, etc.) in data reduction. A comparison of the “push-pull” single-line and global treatments of the flyer data examined above (cf. Fig. 11, Fig. 12) is shown in Fig. 14. The single-time velocity-time plot closely tracks the global acceleration behavior and exhibits considerably less noise than the comparable plot in Fig. 12, particularly at late times. Consistent with well-established advantages in VISAR analysis, the "push-pull" approach applied to reduction of ORVIS image data is much less sensitive to both background light and small-scale fluctuations in reflected light intensity. Also, it is important to note that it is not a requirement to register the lineout data set for each single-line analysis with a fringe center. Considerably finer resolution of small-scale perturbations in velocity can be achieved by extending the analysis to positions between fringes as well. This “rolling push-pull” approach has been used in reduction of the experiments described below. An analogous routine can be used to generate an areal target surface velocity map (at one point in time) from the stop-motion images of the fringe field. In this case, the second spatial dimension substitutes for the time axis (see example calculation in Section VII).

A computer software package that integrates the “rolling push-pull” technique with the necessary image processing methods and an existing VISAR data analysis platform has been developed. Briefly summarized, the typical data reduction procedure is as follows: {a} conversion of image data to standard TIFF format (if necessary), {b} image rotation to level the fringes horizontally (if necessary), {c} definition of a region of interest (ROI) on the image data for further processing, {d} evaluation of average fringe spacing in a region of the image corresponding to no target motion, {e} image expansion and interpolation to adjust the average fringe spacing to a pixel value evenly divisible by four (a step that allows each data set to be registered to either a fringe center or positions 1/4, 1/2, or 3/4 the distance to the center of an adjacent fringe), {f} evaluation of intensity variations along the time axis for positions corresponding to each 1/4-fringe, {g} conversion of these intensity lineouts to a series of equivalent “push-pull” data sets, {h} export of data to the VISAR analysis package to extract velocity-time records corresponding to each 1/4-fringe position and {i} export of velocity-time profiles to a

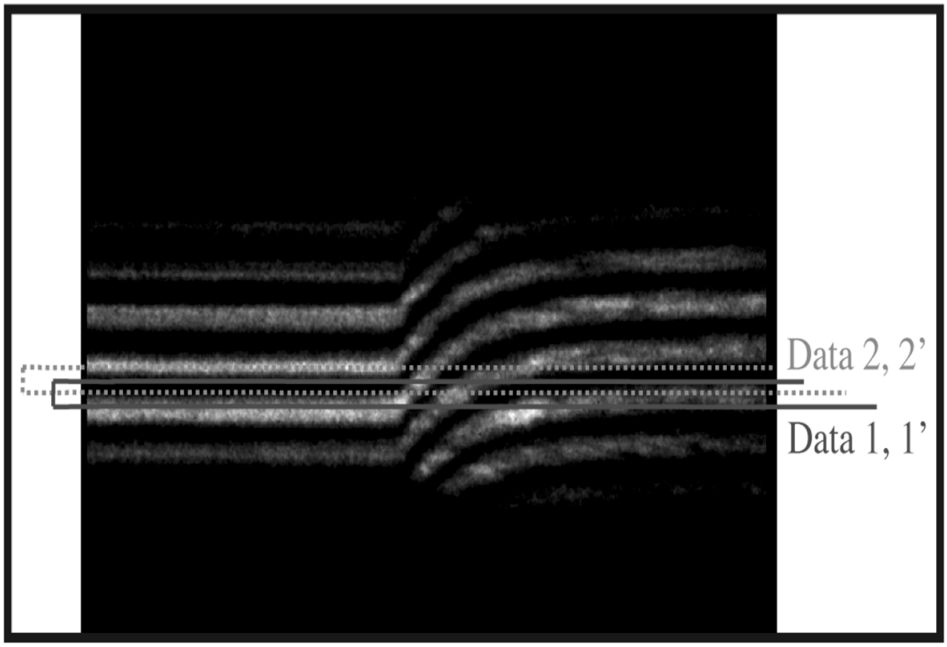

Figure 13. Illustration of intensity "lineout" positions for input to "push-pull" VISAR analysis routine.

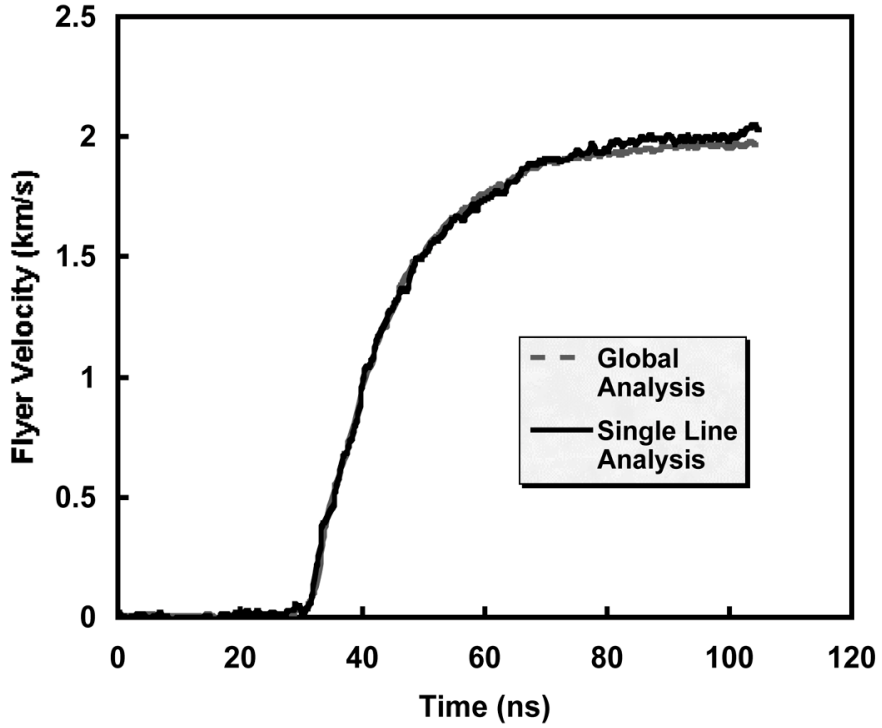

Figure 14. Comparison of velocity-time records obtained from single-line "push-pull" method vs. global data reduction method (see text).

3-D plotting package. The output data is stored in ASCII text format. As a result, simple routines (e.g., in a spreadsheet package) can be used to average or filter the velocity-time plots in various ways, if desired. The software package also includes an optional regression solver to assist in evaluation of fringe spacing for fringes of widely disparate intensities as well as various filters for smoothing the intensity-time data. The key steps in the analysis package are summarized in Fig. 15.

In tests producing relatively modest fringe displacement, it is often necessary to account for systematic drift in the detector sweep (see discussion in Section IV). This drift pattern can be detected in baseline traces (i.e., fringes obtained from a static target). The analysis software provides the option of reducing a baseline record in parallel with a test record, largely accounting for spurious contributions to the velocity-time profiles in the process.

As suggested in Fig. 15, certain methods of image pre-processing may be useful in analysis of the line-imaging ORVIS data. For example, a median filter can be applied to mitigate the effects of "hot" or "dead" spots in the streak camera, intensifier or CCD camera detector. This procedure effectively reduces a significant portion of spurious noise in the velocity-time plots. In certain cases, a Fast Fourier Transform (FFT) filter can be applied to the data with good effect. This method is particularly useful when the signal intensity is very low and contaminated with random noise. FFT enhancement of a noisy, low-intensity ORVIS record of a typical laser-driven flyer launch is illustrated in Fig. 16. It is well known, however, that the bases of Fourier analysis are severely limited in approximating sharp spikes and discontinuities. As a result, important data fluctuations can be suppressed upon application of the FFT filter. Wavelet transforms provide a more specific approach that allows different frequency components to be analyzed with a resolution matched to scale. [18] We are currently investigating the utility of wavelets for processing results in our applications.

IV. SYSTEM EVALUATION EXPERIMENTS

For initial evaluation of the line-imaging ORVIS in gas gun studies, we used a well-characterized symmetric impact configuration in which a 3.25-mm-thick disc of fused silica (backed by carbon foam on an aluminum projectile) impacted a second 5-mm-thick sample of fused silica. Simultaneous line-imaging ORVIS and VISAR measurements of the “free surface velocity” at different spatial locations on the distal face of the target were obtained. For a given impact velocity, the wave profile arriving at this surface can be predicted to high accuracy. The known velocity-time response includes a ramp wave that peaks (after a predictable rise time) to a value matching that of the impact velocity, followed by a rapid unloading that occurs at a time dictated by the sample geometry.

Line-imaging ORVIS results for one test at an impact velocity of 0.245 km-s^{-1} are shown in Fig. 17. Spatial variations in peak velocity as well as details of the velocity-time profile are expected to be negligible in this configuration; however, significant variations in velocity (~0.03-0.05 km-s^{-1}) were observed upon processing of the “raw” ORVIS

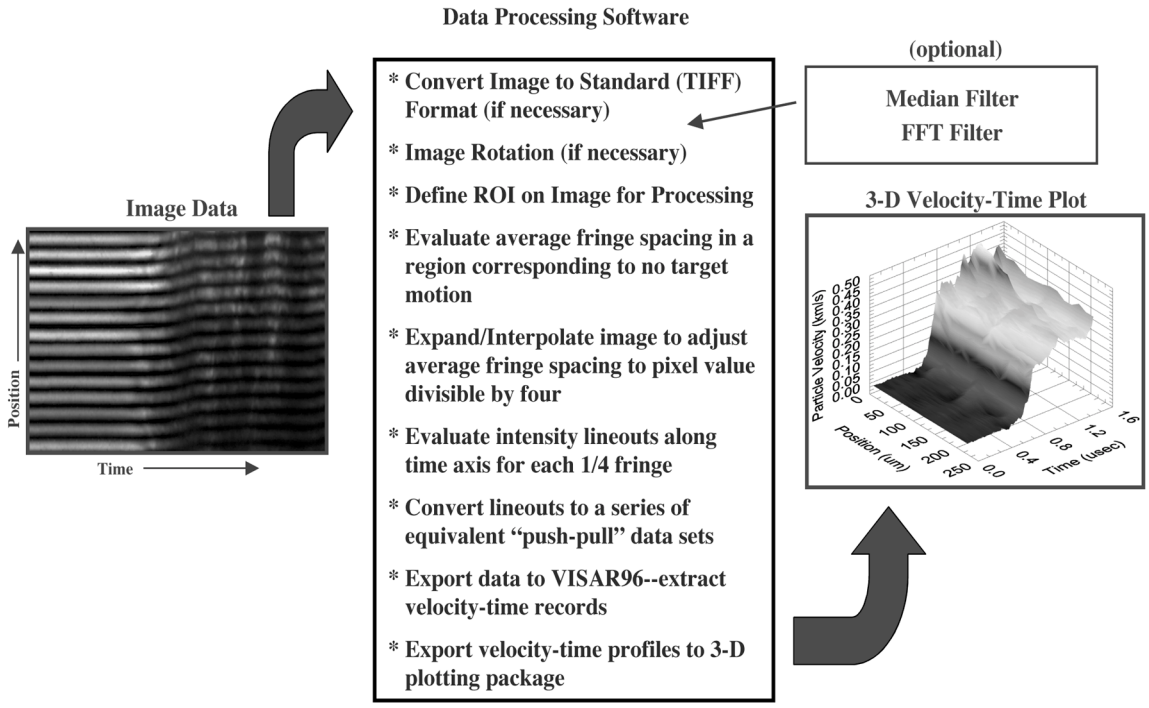

Figure 15. List of important processing steps in software program used to generate spatially resolved velocity-time plots from line-imaging ORVIS data.

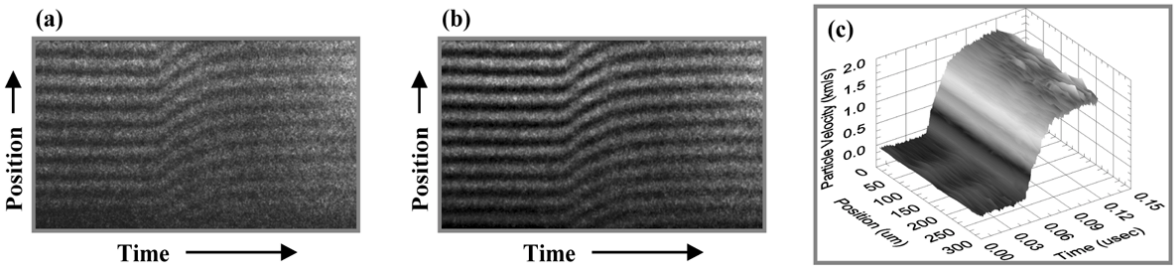

Figure 16. Application of FFT filter to line-imaging ORVIS data: (a) unfiltered, low-intensity fringe record from laser-driven flyer launch; (b) image after FFT filter applied; (c) 3-D velocity-time plot generated by reduction of filtered image.

image data (Fig. 17a). These variations are clearly evident in the plot given in Fig. 17b. Much of this effect was traced to systematic drift in the detector sweep (also clearly observed in baseline traces). This drift pattern is complex but somewhat consistent from shot to shot; the typical correction required is illustrated in Fig. 17c. The reduced ORVIS data in Fig. 17d reflect this correction as incorporated into the analysis routines. Some transverse variation in the velocity-time plot remains after implementing this adjustment; however, the amplitude fluctuation is reduced to ~0.01 km-s^{-1}. The observed temporal behavior (e.g., constant particle velocity under sustained loading) is consistent with expectations based on the experimental geometry (as well as the simultaneous VISAR results). Explanations for the remaining fluctuations include possible sample defects as well as incomplete accounting (shot-to-shot) of the effects of detector drift. The latter issue becomes proportionately less significant when the interferometer velocity-per-fringe constant (VPF) can be adjusted to produce fringe motion over several cycles (vs. approximately half a cycle as shown in Fig. 17a). Other instrumental factors affecting accuracy include the limited spatial resolution of the streak camera (~8 line pairs/mm) and CCD detector (24 pixels per fringe cycle for the record displayed in Fig. 17a). We continue to examine these sources of uncertainty in the data acquisition/reduction process.

The fused silica symmetric impact experiments provided a good test of the velocity response of the interferometer; however, the relatively slow streak camera sweep speed (100 ns-mm^{-1}) needed to capture the interesting features of the wave profile (over a few microseconds) did not effectively test the temporal resolution of this instrument. In fact, the resolution afforded by the CCD camera geometry at this sweep speed corresponds to 4.3ns per pixel. For short duration events, increased camera sweep speeds can be used to record target motion at subnanosecond temporal resolution. This capability has been demonstrated in witness plate studies involving the impact of laser-driven flyers on lithium fluoride (LiF) acceptor windows. [10,19] Figure 18 shows line-imaging ORVIS data for one test of this type (18-μm-thick flyer, impact velocity near 1.7 km-s^{-1}). This event could be viewed at 2 ns-mm^{-1} (corresponding to 0.086 ns per pixel). From analysis of the Hugoniot relationships [20] for aluminum (primary flyer material) and LiF, the particle velocity induced in the acceptor is expected to be ~0.86 km-s^{-1} under these conditions. Accounting for the index of refraction effects [20] in the LiF window, the apparent peak velocity recorded by the interferometer should be ~1.09 km-s^{-1}. The delay leg in the interferometer was set to produce a velocity per fringe constant of 1.093 km-s^{-1}. This value corresponds to a temporal delay of 0.26 ns.

Figure 18 provides a high magnification image of the impact plane (~10 μm per fringe cycle). Prior to flyer impact, the backreflection from the acceptor surface was highly specular. The turning mirror with the central hole was used in this test (cf. Fig. 1) and only a small portion of the reflected light was collected into the interferometer, accounting for the dim pre-impact fringes. Immediate brightening occurred on impact (as the surface became more diffusely reflecting). Consistent with the simple analysis above, the peak fringe displacement was almost exactly one cycle; i.e., ~1.09 km-s^{-1}. The most significant result, however, was the fine resolution of different impact times across this portion of the acceptor, arising from the highly nonplanar geometry of the thin flyer plate.

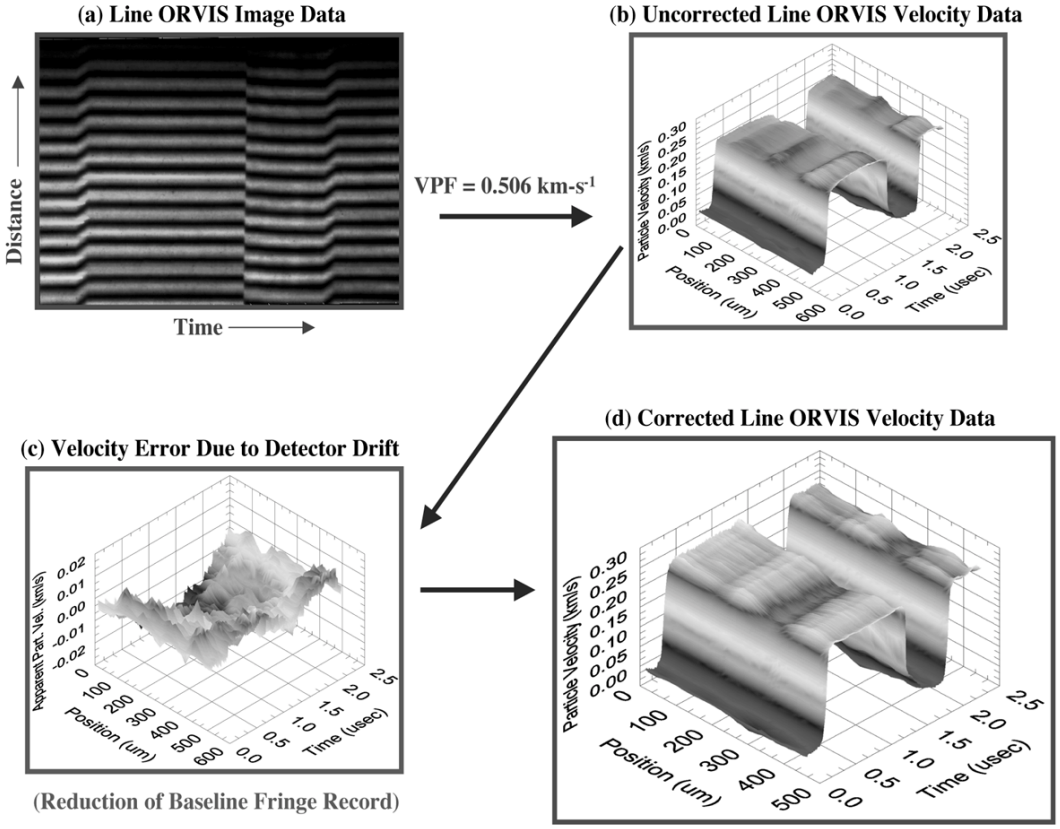

Figure 17. Line-imaging ORVIS measurement of fused silica symmetric impact experiment (0.245 km-s^{-1} impact velocity): (a) ORVIS image data; (b) Reduced data without correction for drift in detector sweep; (c) Typical correction for drift in detector sweep; (d) Corrected spatially resolved velocity-time data.

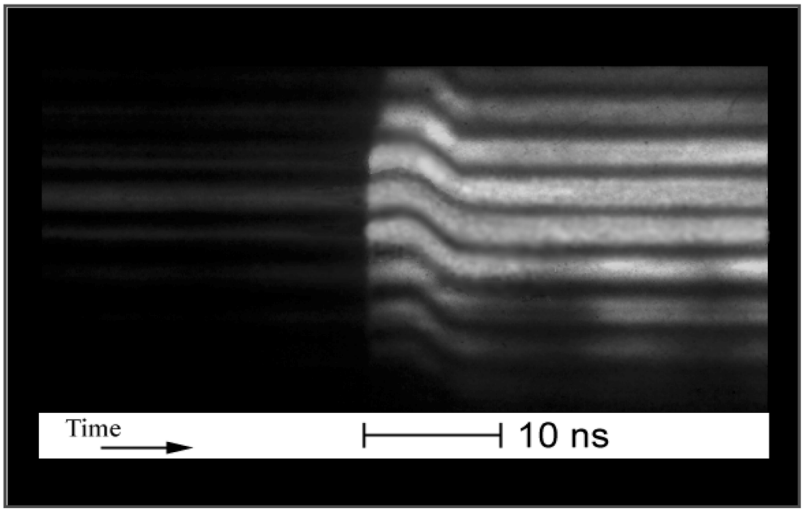

Figure 18. Line-imaging ORVIS record of flyer impact on LiF window (witness plate). Camera sweep speed: 2 ns-mm^{-1}.

The shock jump at each fringe location was recorded in 1-2 pixels (<0.2 ns), roughly consistent with the interferometer temporal delay. Across the full line segment, flyer curvature resulted in >1 ns spread in arrival time. In comparing adjacent fringes, shock jump time differences ~0.2-0.3 ns are clearly evident. The record also shows subtle variations in the pulse shape at each fringe location.

The examples given in this section provide an indication of the capabilities and wide applicability of the line-imaging ORVIS technique. Spatial resolution at mesoscopic scales is easily obtained via high image magnification and reasonable fringe spacing (determined by the interferometer mirror configuration but limited, in practice, by detector size and resolution). On the other hand, the instrument can be configured to examine longer line segments with a corresponding loss of spatial resolution. Available temporal resolution is defined by the required velocity resolution (determined by the temporal delay introduced in the second leg of the interferometer) and is also limited by available streak camera recording times in combination with the CCD camera geometry (i.e., size and number of pixels). The triggering reproducibility of the experiment is also important in this regard. The instrument can be operated using a wide range of velocity per fringe constants, depending on the space available for the interferometer cavity. These characteristics are suitable for examination of a wide variety of heterogeneous materials with different characteristic scale lengths.

V. INVESTIGATION OF LOW-DENSITY SUGAR UNDER IMPACT LOADING

In the study of mesoscopic scale dynamic response of heterogeneous materials under gas-gun-driven impact loading, the preponderance of our efforts has focused on the investigation of pressed, granular sugar as a simulant material for the important explosive HMX. The utility of this candidate simulant has been previously described. [21] Chemically inert to shock loading to fairly high pressures, granulated sugar is reported to be similar in particle size distribution to typical batches of “coarse” HMX (mean particle size ~120 μm) used in various applications. Tests on this material can address mesoscopic scale thermomechanical effects in the absence of complications due to rapid reactions. We have studied low-density pressings of granular sugar with a number of specific goals in mind. First, the spatially resolved results from line-imaging ORVIS can be directly compared to the substantial data base already developed from magnetic gauge (“continuum” response) experiments by Sheffield et al. [21] Second, our tests are intended to provide experimental data for direct comparison and validation of 3-D numerical simulations focusing on the thermomechanical response. [1] Finally, it is useful to explore the behavior of samples prepared with tailored particle size distributions in order to address specifically the effect of this important parameter.

A. Comparison with Magnetic Gauge Studies

Simultaneous line-imaging ORVIS and standard VISAR measurements have been made on the wave transmitted by 4-mm-thick pressed sugar samples in a gas gun target design very similar to that used in the previous magnetic gauge studies; i.e., Kel-F impacting sugar pressed to 65% theoretical maximum density (TMD) in a Kel-F target cup. A schematic diagram of one target design is shown in Fig. 19. This assembly

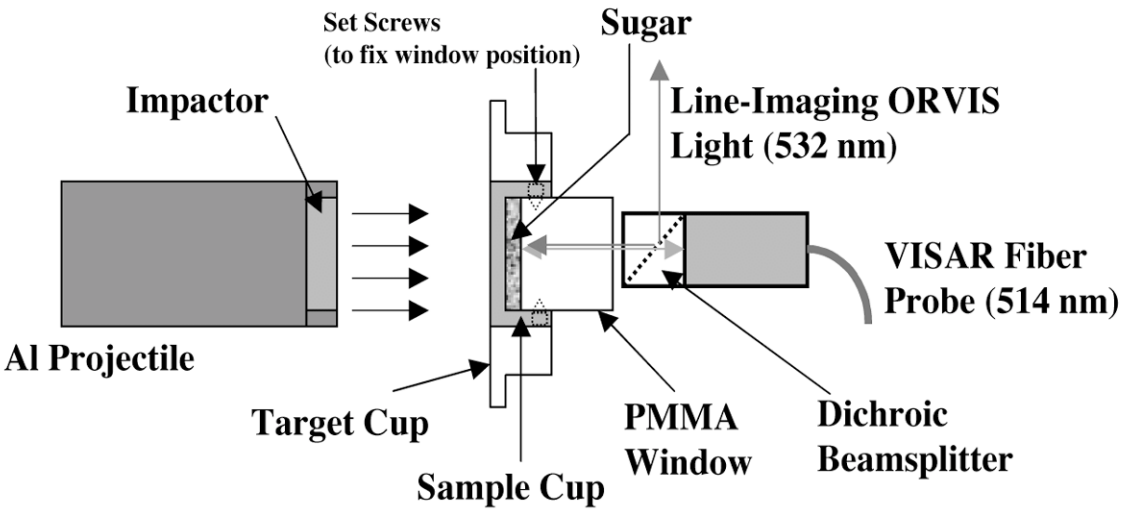

Figure 19. Schematic diagram of gas gun target design for tests on low-density sugar samples. Use of the dichroic beamsplitter enables spatially overlapped as well as simultaneous single-point VISAR and line-imaging ORVIS measurements.

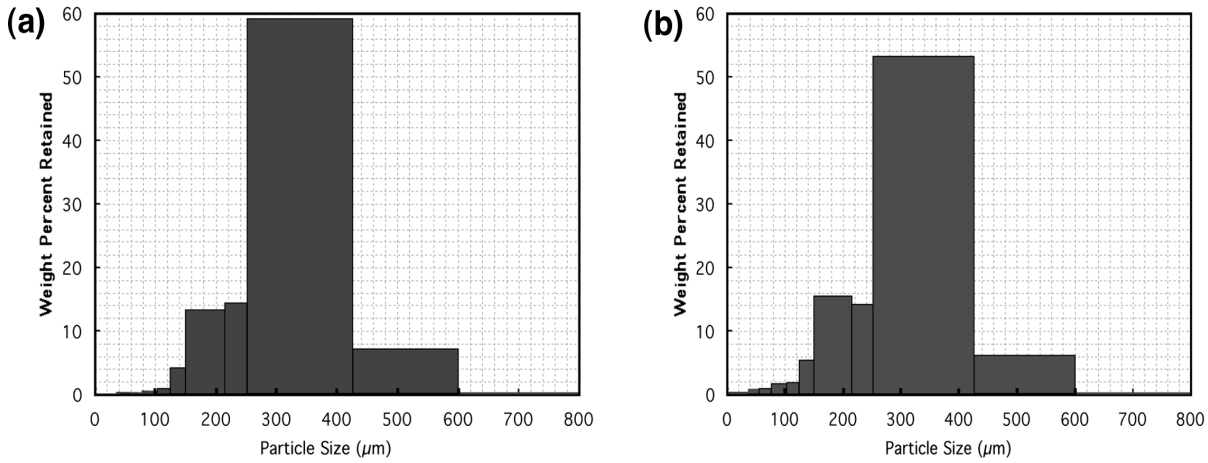

Figure 20. Particle size distributions determined for granulated sugar: (a) As received; (b) After pressing to 65% theoretical maximum density and subsequent release from target cup.

includes the dichroic beamsplitter that accommodates spatial overlap of the ORVIS and VISAR diagnostics. In other tests, we have routed the source illumination for the two techniques to different regions on the sample. Shock arrival at the PMMA interferometer window typically produced severe loss in reflected light intensity when the aluminized window was placed in direct contact with the sugar bed. Accordingly, a 0.225-mm buffer layer of Kapton (placed between the sugar and PMMA) was used in most experiments.

To achieve consistency in preparation of the sugar samples, both mass and volume of granular sugar were carefully controlled. In particular, the desired 4-mm thickness of the sugar bed was maintained using pressing fixtures machined to a tolerance of $\pm$ 0.025 mm. The sugar crystals exhibited a significant elastic response to pressing and release; i.e., the thickness of sugar was observed to increase by 0.1-0.2 mm upon release. To prevent this expansion, the PMMA window was held in place using set screws with sharpened points (cf. Fig. 19). These screws were installed during full pressing.

As part of our sample characterization, we have analyzed the particle size distribution for the sugar used in our tests. In particular we sieved our lot of coarse, granulated sugar under two conditions: (1) as received, and (2) after pressing to 65% TMD (into the Kel-F target cup) followed by release. Results of these operations are shown in Fig. 20a and Fig. 20b, respectively. In both cases the largest weight fraction was found in a very coarse "bin" of material (250-425 μm diameter). In the pressed and released sample, significantly higher weight fractions were observed in the fine-grain (<150 μm) "bins." Hence, the effect of grain crushing is significant even at the low pressing density used in this study.

In tests conducted thus far, impact velocities ranging from 0.32-0.68 km-s^{-1} have been used. Initial results from both VISAR and line-imaging ORVIS are consistent with the systematically varying dispersive behavior of wave profiles seen by Sheffield et al. [21] This includes comparable measured shock and particle velocities as well as very similar rise times in the transmitted wave. The compilation of single-point VISAR data in Fig. 21 demonstrate that the rise times (estimated as the time duration for the transmitted wave velocity to progress from 5% to 95% of the maximum particle velocity level) decrease from 700 ns to approximately 200 ns over the above range of impact velocities. Mesoscopic scale velocity variations (both transverse and longitudinal wave structures) are clearly evident in the spatially resolved ORVIS data, as illustrated in Fig. 22. These records show portions of the transmitted wave manifold for low-density sugar impacted at 0.5 km-s^{-1}. The wave profile under these conditions is typically fairly smooth, as shown in Fig. 22a; however, large-scale fluctuations (such as those displayed in Fig. 22b) are occasionally observed. Rise times can also vary significantly over a line segment. Spatial variations in the observed response undoubtedly depend on the complex details of the size distribution and orientation of crystals as well as voids near the region probed by the optical diagnostics. Experimental and analytical methods that systematically account for the statistical nature of these data are clearly needed to provide a detailed interpretation of the results.

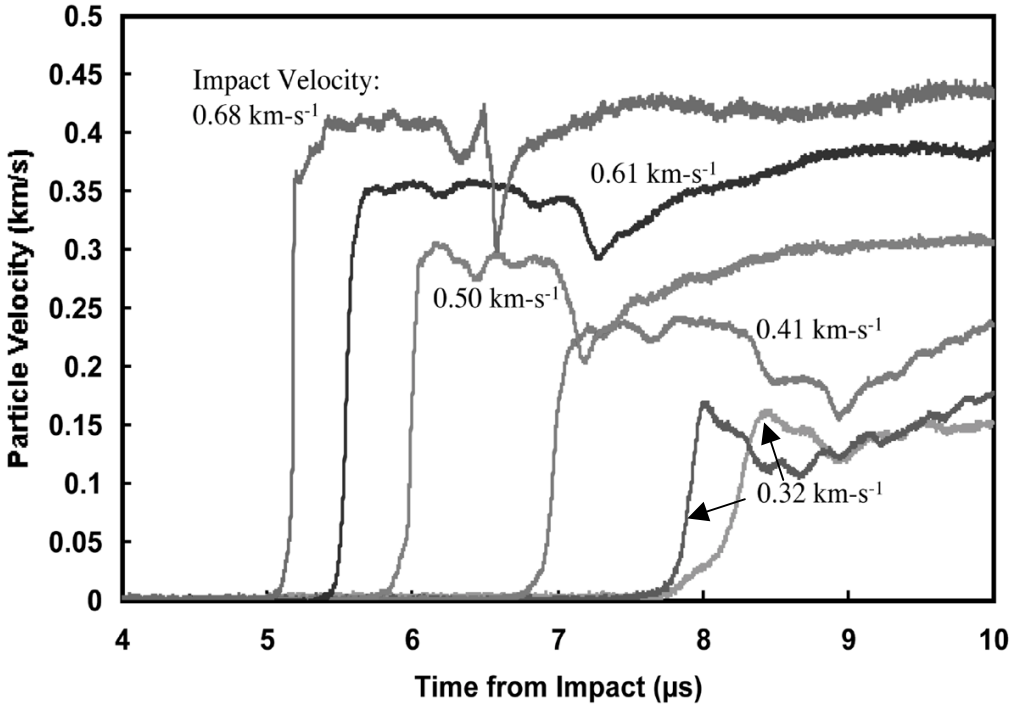

Figure 21. Standard VISAR particle velocity measurements of transmitted waves in shocked samples of coarse, granulated sugar (65% theoretical maximum density); plots illustrate dependence of response on impact velocity.

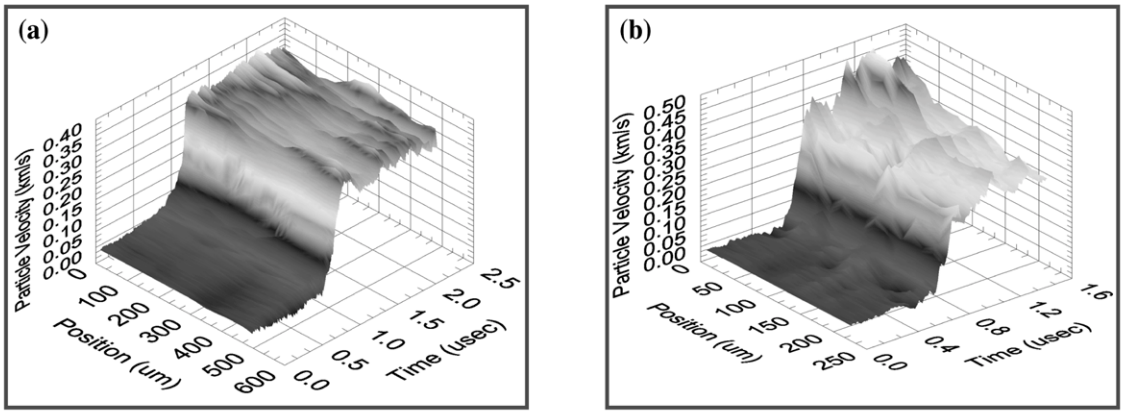

Figure 22. Velocity-time profiles of the wave transmitted through 4-mm-thick bed of low-density sugar; 0.5 km-s^{-1} impact velocity: (a) record displays relatively smooth profile on plateau; (b) record displays high-amplitude fluctuations in one region.

B. Comparison with 3-D Numerical Simulations

Variations in the observed amplitude and frequency of oscillations in the wave profile vs. position provide insight at the mesoscale that should be helpful in defining appropriate material descriptions and interface conditions for detailed computational modeling. [1] For simulation (using the CTH hydrocode) of the response of the low-density pressing of sugar under the impact conditions examined here, the measured particle size distribution of the pressed and released sample (expressed in terms of weight fraction) was converted to an equivalent number density distribution. This distribution was incorporated into packing algorithms described previously [1] in order to generate a random ensemble of sugar crystals consistent with that used in the experiments. Periodic lateral boundary conditions were placed on the computational domain. To achieve a reasonable computation time, it was necessary to restrict the thickness of the sugar crystal ensemble to 2.27 mm. The wave field was transmitted through a buffer layer of Kapton (0.225-mm thick as employed in the experiments) and into the PMMA material used as an interferometer window. Particle velocity was recorded at approximately 50 "tracer" points along a line segment located at the Kapton/PMMA interface.

In the simulations, rapid deformation occurs at material contact points in the sugar. Both stress and temperature fields display a substantial degree of large amplitude fluctuations. These fluctuating fields arise from the effects of shocks interacting with individual material surfaces and multiple crystal interactions. Figure 23 displays a time sequence of temperature fields along a midplane cross-section of a low-density sugar bed subjected to impact at 0.5 km-s^{-1}. Times were chosen to illustrate interesting dispersive wave interaction events at the sugar/Kapton and Kapton/PMMA interfaces. Of particular interest is the material penetration event at the location marked by an arrow in Fig. 23. This effect is also clearly evident in the stress field contours (not shown). Ideally, it would be useful to acquire particle velocity measurements without the attenuating influence of a buffer layer; however, as mentioned previously, we have found that severe loss in the reflected light intensity for both point VISAR and line-imaging ORVIS occurs upon wave arrival at the buffer/PMMA interface when buffer thicknesses <150 μm are used. This observation is consistent with the crystal penetration depth seen in the computations.

Fortunately, the calculated particle velocities retain a significant degree of amplitude fluctuation even after transmission through a 225-μm-thick buffer, as shown in Fig. 24. The 3-D plot of the velocity-time profile at the Kapton/PMMA interface displays complex transverse mode structure in addition to the 120-ns rise time in the wave. Representative plots of the spatially resolved velocity-time field observed by line-imaging ORVIS are also presented in Fig. 24. The record shown in Fig. 24b illustrates the typical behavior of a wave transmitted through a 4-mm-thick sugar sample. Considering the important difference in material geometry, the agreement is reasonably good. In addition to prominent transverse wave structure, both experiment and computations exhibit early peaks in particle velocity (which arise from a shock impedance mismatch between porous sugar and homogeneous buffer material) followed by late-time velocities near 0.25 km-s^{-1}. On the other hand, the observed rise time of the transmitted wave is clearly longer.

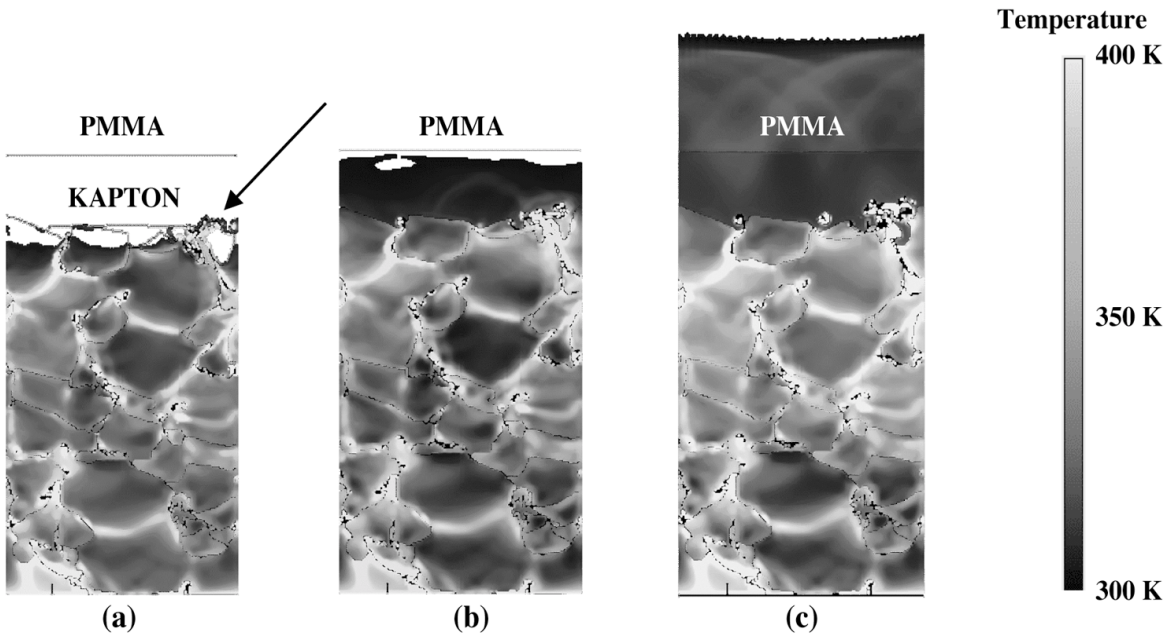

Figure 23. Time sequence of temperature field maps from numerical simulation of low-density sugar under impact loading: (a) initial interaction with Kapton buffer layer; (b) wave approaching PMMA interferometer window; (c) crystal penetration into Kapton layer.

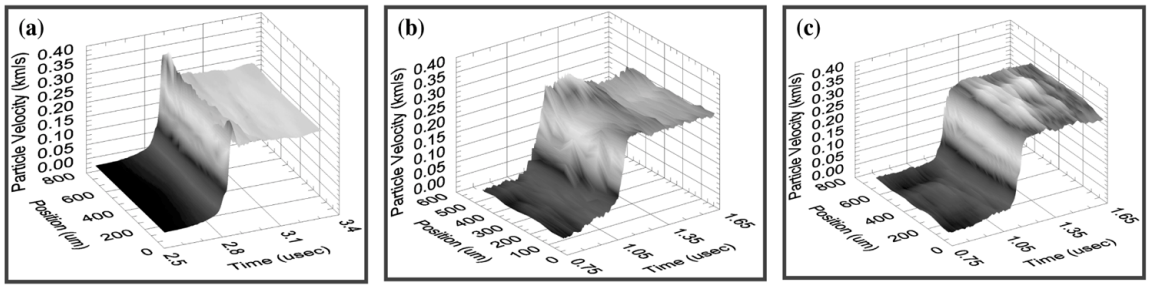

Figure 24. Comparison of (a) results from CTH calculation corresponding to 2.27-mm-thick sugar sample, (b) spatially resolved velocity-time profile of wave transmitted through 4-mm-thick sugar sample, and (c) spatially resolved velocity-time profile of wave transmitted through 2.27-mm-thick sugar sample; impact velocity near 0.5 km-s^{-1}. A 900-ns duration of time is plotted in all three cases.

It is instructive to average the line-imaging ORVIS data over the entire line segment and compare it to the similarly averaged calculated response. This comparison is illustrated in Fig. 25a. Also shown is the point VISAR record obtained in this test (in this case, the VISAR and ORVIS data were acquired at different locations on the target). To aid in the comparison, the traces have been shifted in time to overlap at the 0.1 km-s^{-1} level. The VISAR and ORVIS data are closely correlated in terms of the rise time but significant differences in wave structure are evident on the "plateau" (as might be expected with different probe locations). Both sets of data indicate more dispersion than the calculated result.

The results described above strongly suggest the possibility that the transmitted wave may not be steady at a sugar sample thickness of 2.27 mm. To examine this hypothesis, we prepared and tested several fixtures at the reduced thickness. A plot of the reduced data from one of these experiments is shown in Fig. 24c. The overall response of the 2.27-mm-thick sample is similar to that obtained with the thicker sugar bed; however, the rise time in the transmitted wave is clearly shorter. For additional comparison, ORVIS data (averaged over the entire line segment) for three sugar samples at a thickness of 2.27 mm are plotted along with the averaged calculated result in Fig. 25b. Also shown is a single-point VISAR record (spatially overlapped with the line-imaging ORVIS as illustrated in Fig. 19) from one test. With comparable material geometry, the degree of dispersion indicated by experiment and theory are fairly similar. These results indeed point to non-steady wave behavior at the reduced sample thickness.

Perhaps the most promising aspect of these preliminary comparisons of experiment and theory is that the length scale and spatial resolution afforded by line-imaging ORVIS appear to address the relevant scale for wave fluctuations seen in the numerical simulations. Much work remains to be done, however, in order to obtain a sufficient data base to test many of the critical properties of the computational model. Shot-to-shot variations in the VISAR and ORVIS data described above demonstrate the statistical nature of the measured response of a heterogeneous sugar sample. For each condition of impact velocity, density and particle size distribution, a suitable collection of spatially resolved velocity-time profiles must be acquired in order to sample a sufficient number of crystal/void ensembles to characterize the system properly. Data reduction and analysis methods (e.g., wavelet theory) that allow meaningful statistical variations in the measured response to be separated from noise should be very beneficial in this regard.

C. Preliminary Results with Tailored Particle Size Distributions

Particle size distribution plays a significant role in the dynamic response of low-density sugar to impact loading and initial experiments with tailored distributions have revealed significant differences in the observed behavior of the transmitted wave. For these tests, we prepared two "sieve cut" samples for examination under impact loading: (1) a coarse cut sample using the predominant 250-425 μm fraction (cf. Fig. 20a), and (2) a relatively fine-grain sample using only 150-212 μm particles. Significantly higher force was required to press the coarse-grain sample to 65% TMD as a result of its restricted ability to pack uniformly. A substantially larger extent of grain fracturing (leading to a

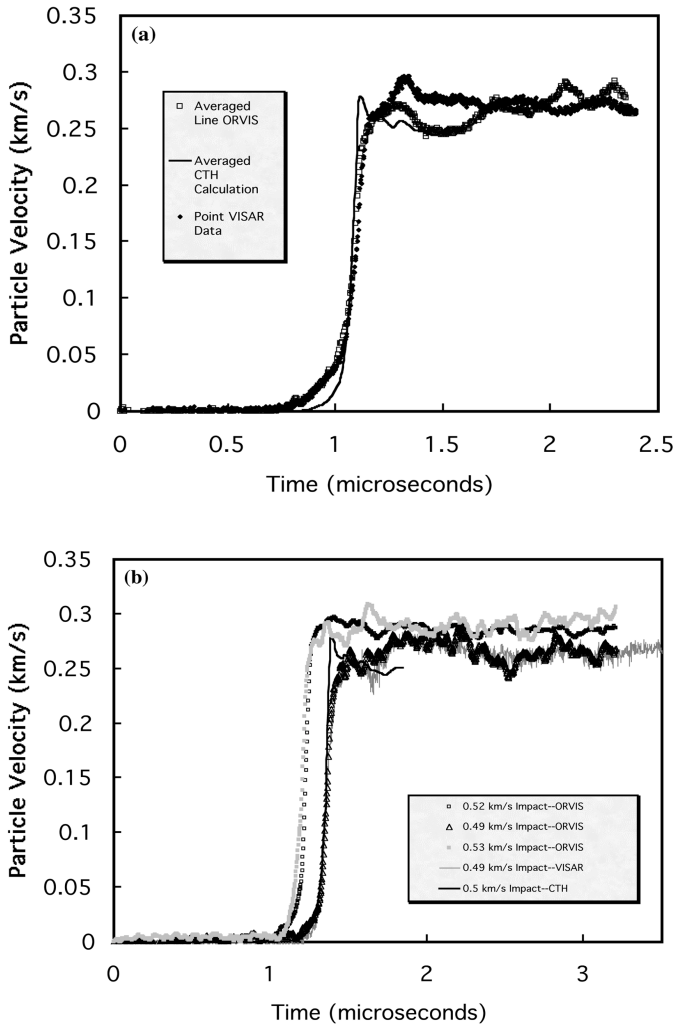

Figure 25. Comparison of point VISAR and averaged line-imaging ORVIS data to averaged response from numerical simulation: (a) 4-mm-thick sugar data vs. computation; (b) 2.27-mm-thick sugar data vs. computation.

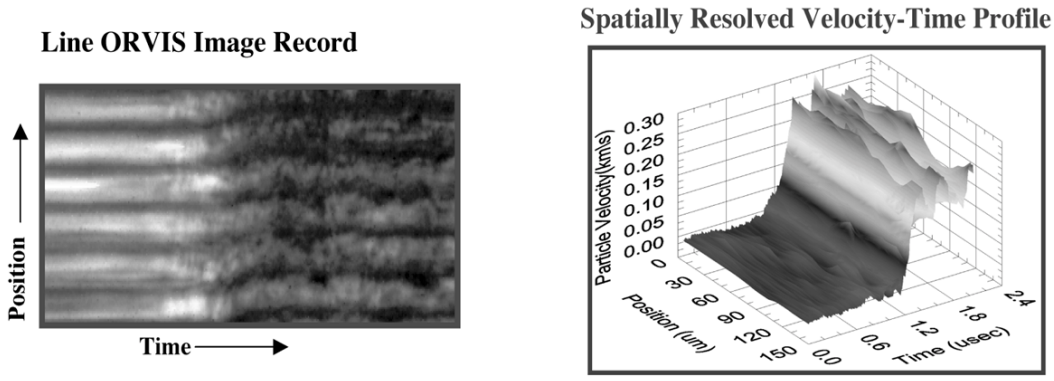

Figure 26. Transmitted wave profile from coarse-grain sugar sample (as measured by line-imaging ORVIS).

larger fraction of fine-grain particles generated in the pressing process) is very likely in this case. The two pressed samples (both 4-mm-thick) were examined upon impact at 0.42 km-s^{-1} using simultaneous line-imaging ORVIS and single-point VISAR (not spatially overlapped in these tests).

Line-imaging ORVIS data for the coarse- and fine-grain samples are shown in Fig. 26 and Fig. 27, respectively. The corresponding VISAR velocity-time records along with a VISAR trace obtained using a sugar sample with the normal particle size distribution (cf. Fig. 20b) are displayed in Fig. 28. Both diagnostics indicate more dispersive wave behavior in the coarse grain sample. In particular, the ORVIS and VISAR wave profiles in this case exhibit significantly longer rise times as well as generally higher amplitude oscillations. The general trend of longer rise times for coarser samples has been previously observed in magnetic gauge studies of shock-loaded sugar and HMX [22] The increased sample heterogeneity arising from grain fracturing during pressing may also contribute to the dispersive nature of the coarser sample. An expanded data base of results on samples with tailored particle size distributions should provide insight into the properties driving dispersive behavior and provide informative tests of the accuracy of mesoscopic scale numerical simulations.

VI. PRELIMINARY EXPERIMENTS ON LOW-DENSITY HMX

The need for much additional insight into microstructural properties driving initiation and reaction growth in pressed, granular explosives is an important application that may be addressed by spatially resolved velocity interferometry in concert with detailed 3-D numerical simulations. The capacity for resolution at mesoscopic scales in both experiment and computational modeling is important in unraveling the critical physical and chemical phenomenology. We have begun a preliminary investigation of wave propagation through low-density HMX to assess the capability of line-imaging ORVIS in this research area.

The current understanding of shock loading of porous explosives at the level of continuum measurements has been examined in detail in a recent review by Sheffield et al. [22] This review provides a helpful background for the work described here. In magnetic gauge studies of low-density (65-74% TMD) HMX, Sheffield et al. have shown that compaction waves at levels below the threshold for reaction in the porous explosive behave in a manner similar to those measured in low-density pressings of sugar. The transmitted waves are spatially and temporally diffuse. Rise times for waves transmitted through 3.9-mm-thick samples of coarse-grained HMX (mean particle size near 120 μm) increase as the loading projectile velocity decreases, ranging from 100 ns (at impact velocity > 0.5 km-s^{-1}) to 500 ns (at impact velocity < 0.3 km-s^{-1}). Rise times in pressings of fine-grained HMX (mean particle size near 15 μm) are typically much shorter (<100 ns over the full range of impact velocities). At levels above the threshold for initiation, chemical reaction causes the wave to accelerate and to become steeper as it travels. The observed transmitted wave behavior is a complex function of both pressing density and particle size distribution. Consistent with the conventional understanding on explosive

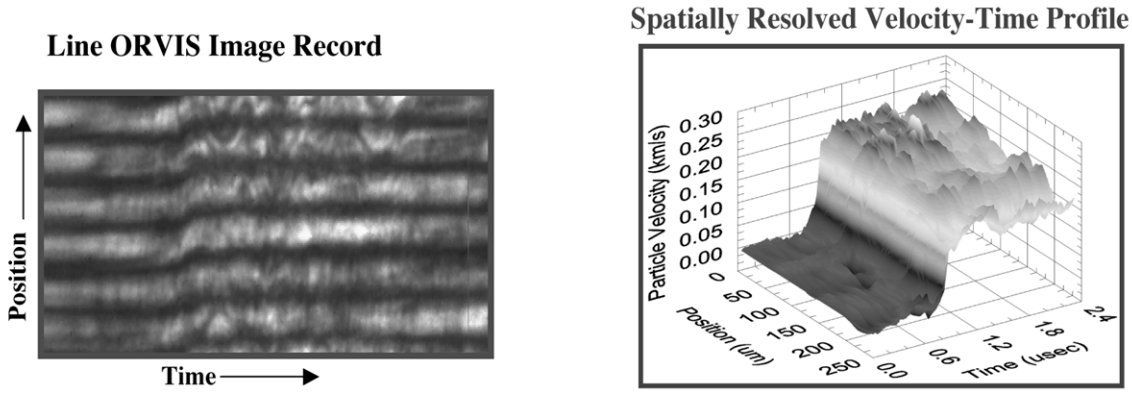

Figure 27. Transmitted wave profile from fine-grain sugar sample (as measured by line-imaging ORVIS).

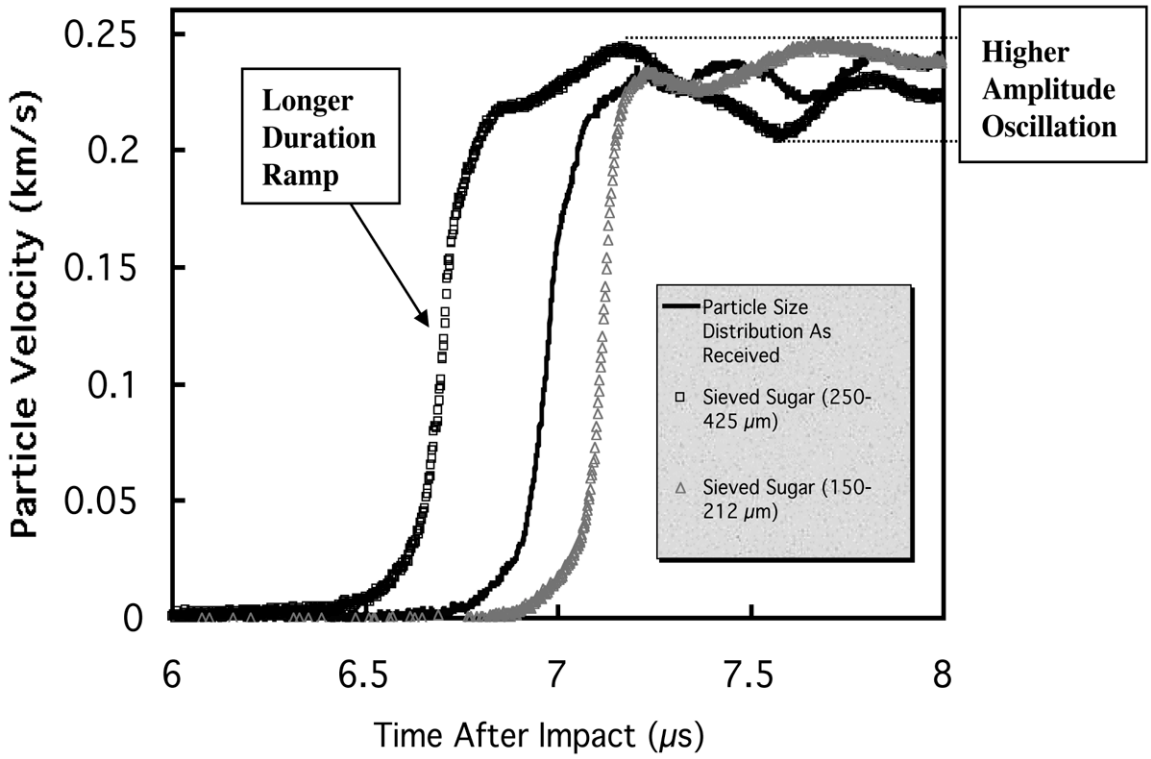

Figure 28. Effect of grain size on transmitted wave profiles for low-density sugar (as measured by standard VISAR); impact velocity near 0.42 km-s^{-1} in all cases.

sensitivity, HMX pressings at higher density were found to be generally less sensitive. Reaction also occurs at a much lower loading pressure in coarse-grained HMX than in fine-grained HMX. Once reaction is initiated in the fine-grained HMX, however, chemical energy release occurs much more rapidly. These observations support the long-standing qualitative picture of heterogeneous explosive initiation via hot spot formation and grain burning. In coarse materials, hot spots are relatively large and persistent, leading to initiation at low input pressures. In the case of finer materials, hot spots are more numerous but much smaller and subject to rapid cooling, resulting in less sensitivity overall. On the other hand, grain-burning models in which the rate of reaction depends on particle size and surface area predict a very rapid reaction growth once reaction begins to spread in the fine-grained explosive.

To explore the effects of initiation and reaction growth at mesoscopic scales in low-density HMX, we have prepared and tested gas gun targets similar to that represented schematically in Fig. 19. For direct comparison to the magnetic gauge experiments on coarse-grained HMX described above, we used powder from an identical lot of Holston batch HOL 920-32. As mentioned previously, this material is characterized by a mean particle size near 120 μm. The HMX was pressed into Kel-F target cups to a density of 65% TMD (1.24 g-cm^{-3}) and to a depth of 4 mm.

A spatially resolved velocity-time profile for low-density HMX subjected to impact at 0.4 km-s^{-1} is shown in Fig. 29. In many respects, the transmitted wave profile is very similar to that induced in low-density sugar (cf. Fig 22). The observed rise time of the diffuse wave is 150-200 ns, slightly faster than that reported by Sheffield et al. [22] In contrast to results from the sugar experiments, the 3-D plot in Fig. 29 also displays a slow but systematic increase in velocity subsequent to the initial ramp. This wave growth indicates the onset of exothermic chemical reaction in the HMX. Substantial differences in wave amplitude as a function of position (transverse to the direction of wave propagation) are also evident in this record. Increasing the impact velocity to 0.53 km-s^{-1} results in rapid reaction of the low-density HMX, as displayed in Fig. 30. In this case, the transmitted wave has steepened to a near instantaneous shock jump and the maximum particle velocity has grown to near 1.0 km-s^{-1}. Significant amplitude fluctuations are evident on the wave profile. It is interesting that many of these fluctuations appear to be high frequency events temporally and yet distributed over a fairly wide distance (~1 mm) in the transverse spatial dimension. Results of this type should provide useful tests of the chemistry models employed in 3-D numerical simulations of explosive initiation at the mesoscale. Toward this end, we intend to develop a more comprehensive data base on the response of the Holston 920-32 HMX formulation, utilizing a wider range of impact conditions as well as testing for reproducibility. These results will be supplemented by a limited number of tests on "sieve cut" (narrow particle size distribution) HMX samples.

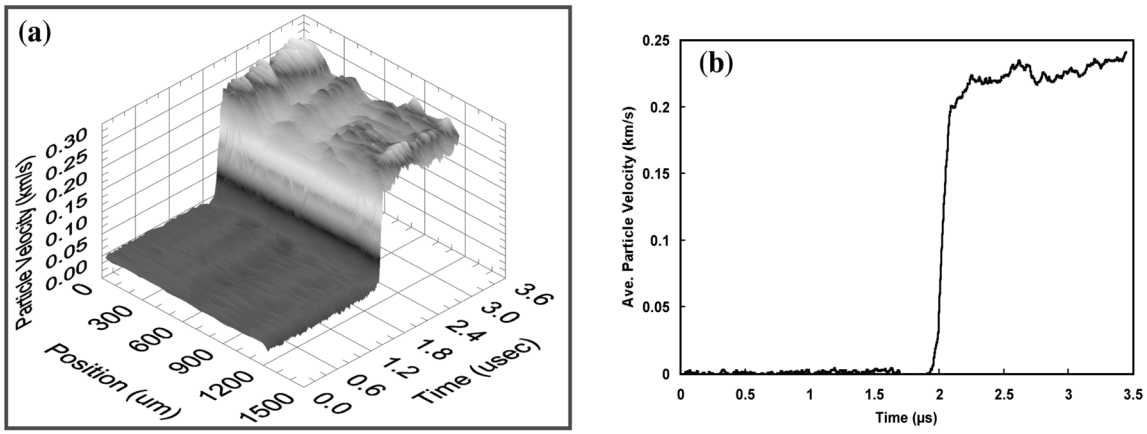

Figure 29. Transmitted wave profile from low-density HMX sample; 0.4 km-s^{-1} impact velocity: (a) spatially resolved velocity-time results from line-imaging ORVIS; (b) particle velocity vs. time averaged over the complete line segment.

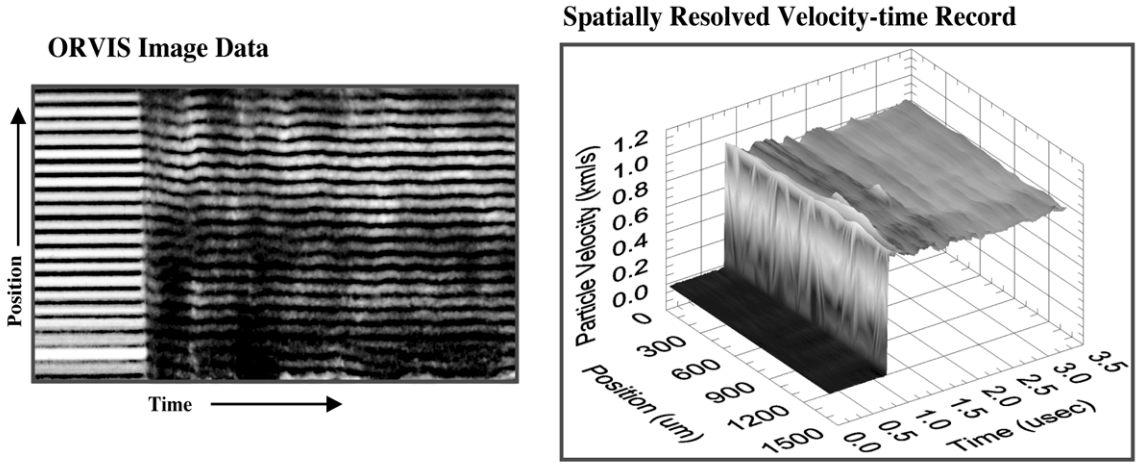

Figure 30. Transmitted wave profile from low-density HMX sample; 0.53 km-s^{-1} impact velocity: (a) image data showing abrupt velocity jump; (b) spatially resolved velocity-time results.

VII. APPLICATION OF LINE-IMAGING ORVIS TO OTHER EXPERIMENTAL SYSTEMS

In the course of developing line-imaging ORVIS as a diagnostic for spatially resolved, mesoscopic scale studies of wave propagation in heterogeneous explosive and inert surrogate materials, we have had the opportunity to evaluate these techniques on a variety of other interesting systems as well. In this section we briefly describe results from a few of these applications, including (1) multidimensional shock wave phenomena in Z-cut sapphire, (2) incipient spall in thin tantalum discs, (3) foam reverberation experiments, (4) complex shock response in samples of glass-reinforced polyester, and (5) analysis of the dynamic behavior of laser-driven flyers. The data presented here are intended primarily to illustrate the utility of the line-imaging ORVIS technique as a probe of material response in these systems. Detailed analysis and discussions of the various experiments will be presented elsewhere. Important recent applications of line-imaging ORVIS not described in this report include studies of multidimensional wave propagation in ALOX and PZT materials in support of neutron generator power supply development as well as critical diagnostic support of radiation-drive experiments on the Z accelerator at Sandia National Laboratories.

A. Spatially Resolved Velocity-time Profiles from Z-Cut Sapphire

The mesoscopic scale spatial resolution afforded by line-imaging ORVIS presents many interesting opportunities for efficient probing of complex, multidimensional shock effects in well-characterized homogeneous materials such as single-crystal sapphire (Al_2O_3) discs prepared with axis parallel to the crystallographic Z-axis. A series of symmetric impact experiments have been performed on sapphire samples in a test configuration shown schematically in Fig. 31. The impactor discs were 10 mm thick and 31.8 mm in diameter, respectively. The sapphire targets were 5.1 mm thick and 50.8 mm in diameter, respectively. ORVIS measurements were made at the distal free surface of the sapphire acceptor. This surface was prepared with a very thin reflective coating of aluminum. Impact velocities ranged from 0.295 to 0.794 km-s^{-1}. For these tests, the ORVIS optics were configured to generate a low magnification image at the detector, resulting in a line segment probe spanning 13 mm.

Results of one experiment performed at an impact velocity of 0.564 km-s^{-1} are presented in Fig. 32. The center of the line segment probe was deliberately positioned a few mm off-center in this test. At the low magnification employed, the transverse distance corresponding to one fringe cycle is approximately 550 μm. The image data (Fig. 32a) reveal many interesting details. Significant tilt of the impactor is indicated by the systematic increase in shock arrival time from bottom to top in the image. Edge relief waves proceeding toward the axis of the target disc are clearly visible as disturbances in the fringe intensity. Complex and apparently asymmetric variations in the spatially resolved particle velocity follow the arrival of this edge relief. These variations may indicate the presence of some crystal anisotropy and may be influenced by the projectile tilt. Finally, a distinct, late-time unloading event arising from wave interaction at the aluminum/sapphire interface on the projectile (and subsequently propagating to the free

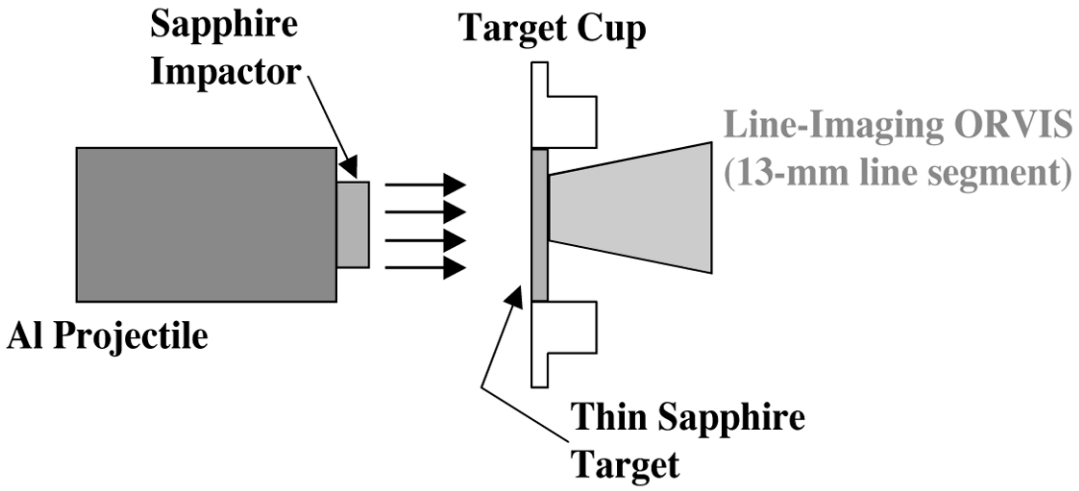

Figure 31. Schematic diagram of gas gun target design for symmetric impact experiments on Z-cut sapphire.

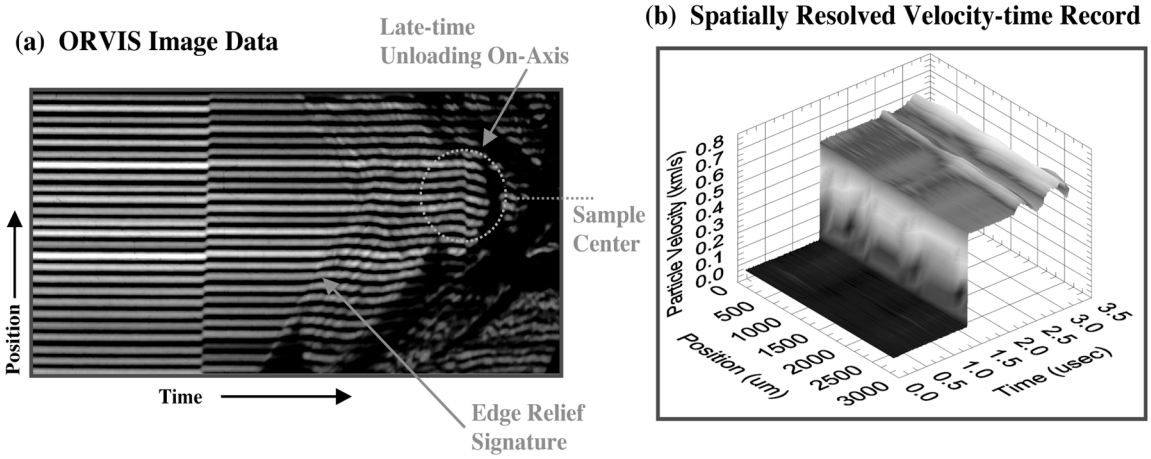

Figure 32. Line-imaging ORVIS probe of multidimensional effects in the symmetric impact of Z-cut sapphire--0.564 km-s^{-1} impact velocity: (a) image data spanning 13-mm-long line segment; (b) velocity-time profile for 3-mm-long segment near the center of the target.

surface) is evident in the fringe data near the sample center. A spatially resolved velocity-time plot from this region in displayed in Fig. 32b. Much additional experimentation and analysis are needed to provide a satisfactory interpretation of the material behavior revealed by our initial tests.

B. Spall Studies in Tantalum

The investigation of spall and fracture of materials under dynamic loading is an extremely rich topic of inquiry. Continuum-level experiments and model descriptions have been widely and successfully applied to many problems in this research area; however, in recognition of the inherently heterogeneous nature of time-dependent void and crack growth in shock-loaded materials, there has been considerable recent effort to quantify these processes at the mesoscale. [23] Combined with the potential of metallurgical examination of recovered samples, the ability of line-imaging ORVIS to probe material motion along a line segment represents a productive new approach to the investigation of incipient spall.

We have explored this application in symmetric impact experiments using a very thin (0.45-mm-thick) disc of tantalum to impact a 1.95-mm-thick target of the same material. This configuration was designed to generate hydrodynamic tension and spall in the acceptor at a plane located <1 mm from the free surface (line-imaging ORVIS measurement plane). An image record for an experiment at an impact velocity of 0.26 km-s^{-1} is shown in Fig. 33. This input condition was designed to be slightly above the known spall threshold for commercial-grade tantalum. The image data reveal significant differences in the velocity-time profile across the 2-mm-long line segment. Toward the top of the image, rarefaction wave interaction produces nearly complete unloading and particle velocity is reduced to a value near zero. At positions corresponding to the bottom of the image, however, substantial reverberations after the initial loading pulse are evident. These local differences in velocity-time behavior are illustrated in the plot displayed in Fig. 34. The observed fluctuations likely correspond to local variations in the size and location (relative to the measurement plane) of voids or cracks induced by impact and release. The distance scale corresponding to significant variation in the velocity-time profile is on the order of a few hundred micrometers, consistent with void sizes inferred from other dynamic experiments. [23] Similar variations in the spatially resolved velocity-time record have been observed at an impact velocity of 0.36 km-s^{-1}.

C. Foam Reverberation Experiments

In applying line-imaging ORVIS to the investigation of the mesoscopic scale response of another type of heterogeneous material, we tested a configuration in which low-density foam (6.3-mm-thick) impacts a thin (1-mm-thick) aluminum witness plate. Measurements at the free surface of the aluminum typically show a steady "ring up" of velocity with superimposed features arising from the detailed microstructure of the high-porosity foam. Due to the compact geometry of the ORVIS assembly employed in these tests, we were restricted to optical delay cylinders <10 cm in length, resulting in a practical lower limit of ~0.5 km-s^{-1} for the velocity-per-fringe constant (VPF). The

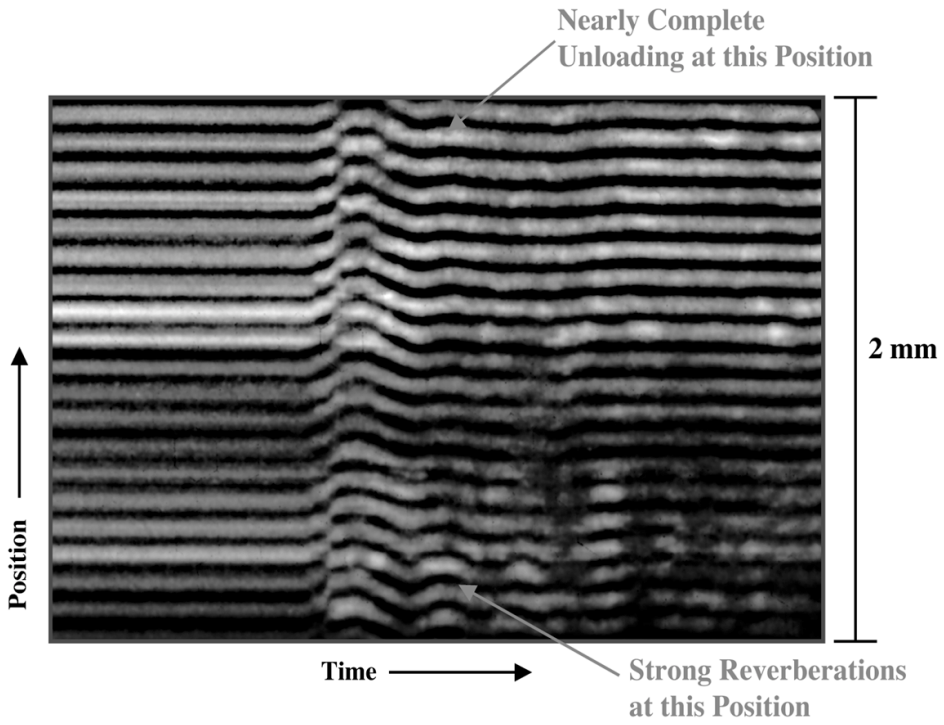

Figure 33. Line-imaging ORVIS record of incipient spall phenomena in symmetric impact of tantalum; 0.26 km^{-1} impact velocity.

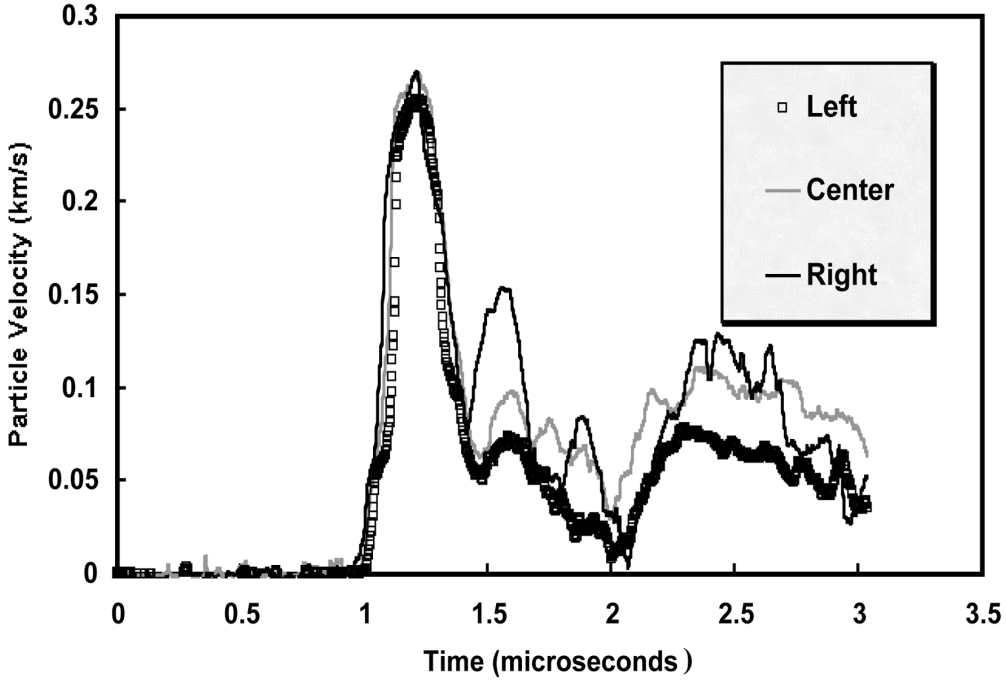

Figure 34. Particle velocity vs. time at three different regions in tantalum spall experiment probed by line-imaging ORVIS. "Left" and "right" correspond to regions near the top and bottom, respectively, of the image shown in Fig. 33.

limited recording time of the particular streak camera/intensifier/CCD camera detector combination used in these experiments proved to be an additional constraint, limiting data collection to a period <2.5 μs. The growth in free surface particle velocity is typically very gradual in the wave reverberation test configuration, corresponding to approximately 60 m-s^{-1} per microsecond for impact at 0.83 km-s^{-1}. Hence, our system was relatively insensitive to the small fluctuations expected in these experiments. Nevertheless, we were able to observe considerable detailed structure in the low-amplitude spatially resolved image data, as shown in Fig. 35a. The velocity-time profile derived from this data is displayed in Fig. 35b. While the profile is relatively noisy as a result of low instrumental sensitivity to the very small changes in velocity, significant variations across the line segment are evident. The averaged response determined by the line-imaging ORVIS was consistent with the simultaneous single-point VISAR record obtained at a different measurement location in this test. With a properly configured instrument (lower VPF, longer recording times), detailed studies of the mesoscopic scale wave structure in this experimental system should be readily achievable.

D. Glass-Reinforced Polyester Experiments

Another heterogeneous material examined under impact loading was a glass-reinforced polyester (GRP) composite. This material features an extremely complex geometry of very fine glass fibers that are bundled in strands which, in turn, are woven roving in a polyester resin matrix. A thick (25-mm) fused silica impactor was used in these tests. The wave transmitted by 3.2-mm-thick samples of the GRP composite was passed through a thin (~1-mm-thick) PMMA buffer and examined at the interface of this buffer with a PMMA interferometer window. An illustrative case of the spatially resolved response of the GRP is shown in Fig. 36. Several effects are evident including a systematic difference in shock arrival time with position (~60 ns over a transverse distance of 2 mm, a time duration far in excess of the difference arising from impact tilt alone), high-amplitude reverberations in the wave profile, and the occurrence of severe loss in reflected light over certain regions of the image record. These effects reflect the complex periodic geometry of this sample that leads to a highly structured transmitted wave with resonance-like behavior. Effects of this type (including widely varying particle velocities depending upon measurement probe position) are clearly indicated by detailed numerical simulations using a realistic approximation to the weave geometry and component material properties. [24]

E. Dynamic Behavior of Laser-Driven Flyers

Experimental methods for generating laser-driven flyers provide a promising approach to the development of a laboratory-scale capability for many quantitative studies of material response to shock loading. The dynamic behavior of these laser-accelerated plates is an important factor in determining their utility for this application. In addition to providing acceptable planarity on impact, it is essential that the flyer arrive at the impact plane either fully intact and at solid density or with dynamic physical properties that can be adequately characterized in a time-dependent manner. Line-imaging ORVIS provides an effective tool for evaluating flyer performance. As indicated

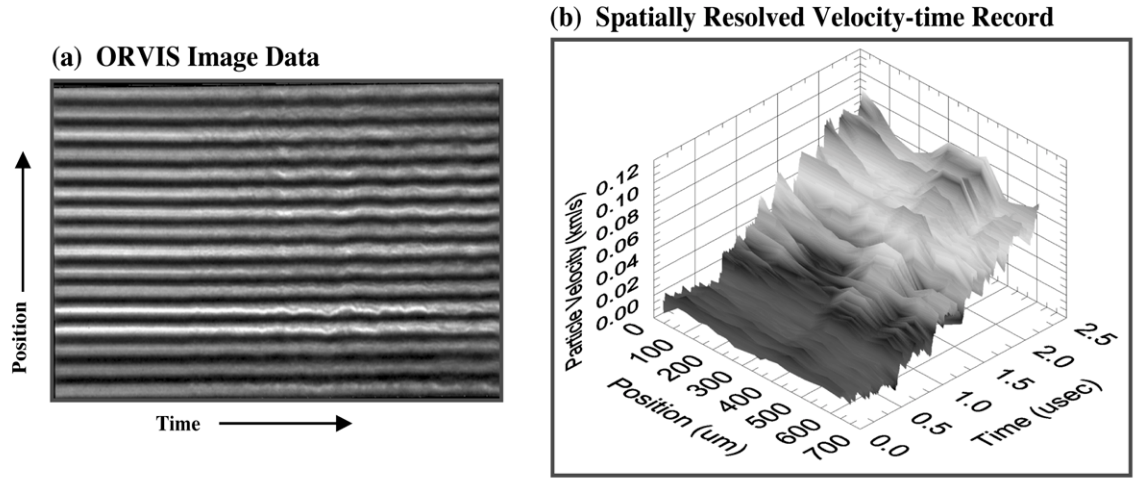

Figure 35. Line-imaging ORVIS record from foam reverberation experiment: (a) image data showing slow growth in particle velocity vs. time and numerous low-amplitude fluctuations; (b) spatially-resolved velocity-time profile exhibiting complex response.

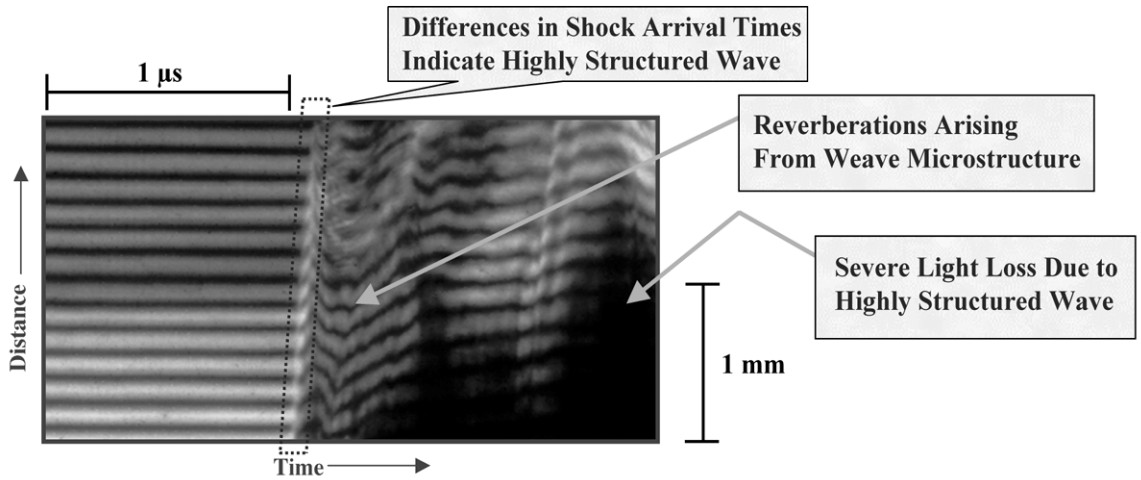

Figure 36. Line-imaging ORVIS record illustrating complex wave transmission through shock-loaded glass-reinforced polyester composite.

previously, acquisition of simultaneous stop-motion images of the full fringe field provides a complementary diagnostic for analyzing flyer behavior.

A line-imaging ORVIS record for an 87-μm-thick, 800-μm diameter flyer launched using a 69 mJ, 18-ns duration pulse from a Q-switched Nd:Glass laser driver is shown in Fig. 37a. The image displays the typical pattern of reflected light loss that begins at the edge of the flyer and progresses toward the center (cf. fringe record in Fig. 1). This pattern arises from more rapid acceleration near the flyer center, resulting in a significant bow in the flyer plate geometry. The velocity-time profile exhibited by the center portion of the flyer is displayed in Fig. 37b. The individual velocity-time records comprising this profile can be integrated to generate the corresponding displacement-time profile, shown in Fig. 37c. Only small displacements are evidently required to produce the light loss regions seen in the image data. This effect arises (at least in part) from the relatively high f-number of the ORVIS collection optics combined with a relatively strong specular component of target surface reflectivity.

The generation of a 2-D velocity map from a stop-motion image of the fringe field is illustrated in Fig. 38. The flyer target in this case was an 18-μm-thick coating of aluminum that was vapor deposited on the output face of a 400-μm-diameter optical fiber. Figure 38a shows an image of the fringe field superimposed on the image of the flyer target at rest. Upon injection of the driving laser pulse into the fiber, the target is accelerated from the fiber face. Figure 38b displays an image of the displaced fringe field captured early in the launch process. An intensifier gate time of 3 ns was used to "freeze" the fringes at this point in time. Rapid deformation of the flyer at the target perimeter results in substantial loss of reflected light even at this early interval in the acceleration process. Nevertheless, regions with reasonable fringe intensity and contrast may be analyzed using the methods outlined in Section III. To implement this analysis, the fringe image is rotated by 90^{o} (as shown in Fig. 38b) and the second distance axis (with appropriate calibration of the image magnification) is treated in the same manner as the time axis in streak images. A baseline image (i.e., of the flyer at rest) must be analyzed in tandem with the data image to account properly for fringe curvature. In addition, some portion of the data image corresponding to a region at rest must be included in the analysis to establish the zero velocity level. An areal velocity plot derived from this method is shown in Fig. 38c. An informative picture of flyer curvature (particularly near the target center) emerges from the data. Unlike typical streak camera data, fringe field images from diffuse targets exhibit a high degree of speckle in both spatial dimensions. This can result in a relatively noisy velocity map. We are continuing to evaluate methods for optimizing the process in reducing this type of image record.

VIII. CLOSURE

Relatively straightforward changes in the optical design of a conventional optically recording velocity interferometer system (ORVIS) can be used to produce a line-imaging velocity interferometer wherein both temporal and spatial resolution can be adjusted over a wide range (subject to various limitations arising from detector characteristics). As a

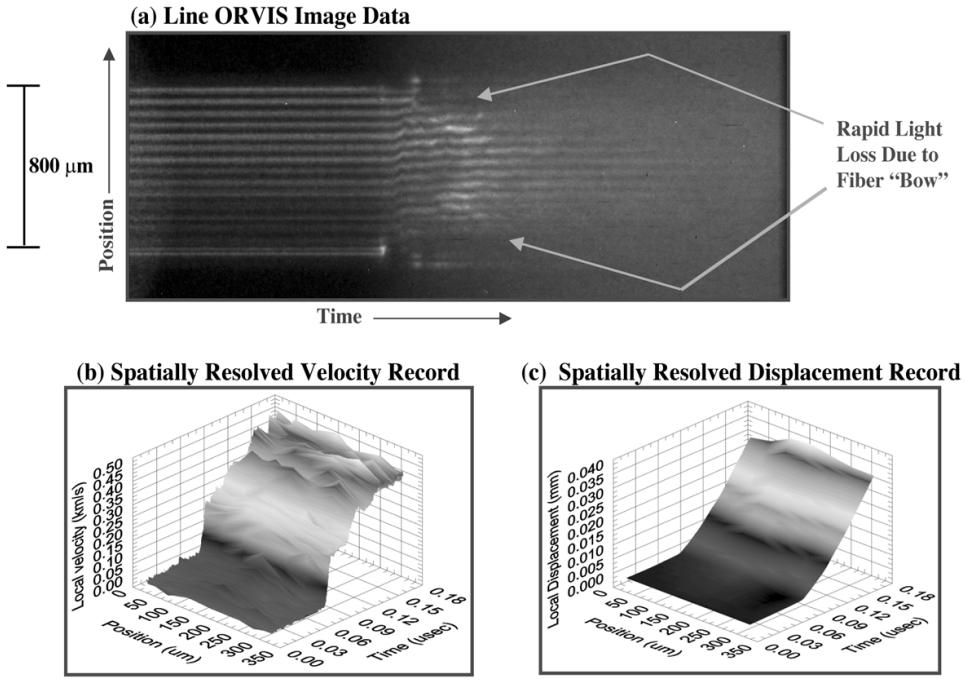

Figure 37. Line-imaging ORVIS record illustrating dynamic behavior of laser-driven flyer: (a) image data showing velocity history of flyer plate free surface; (b) spatially resolved velocity-time profile near the center of the target; (c) spatially resolved displacement-time profile illustrating development of "bow" in flyer plate geometry.

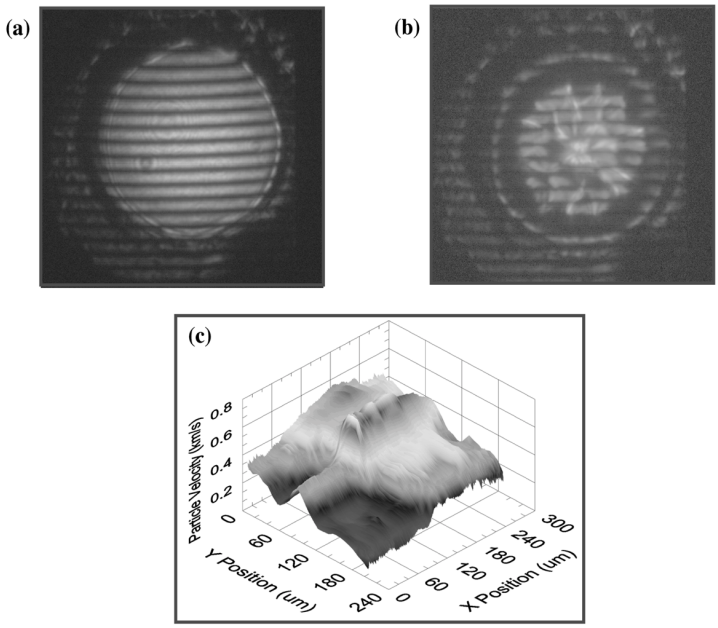

Figure 38. Analysis of 2-D velocity field at one point in time during acceleration of laser-driven flyer: (a) fringe field for flyer target at rest; (b) stop-motion image of fringe field during flyer launch; (c) spatially resolved velocity map of flyer free surface at instant of image capture.

result, line-imaging ORVIS can be tailored to a variety of specific applications involving dynamic deformation of heterogeneous materials as required by the characteristic length scale of these materials. Many types of multidimensional and statistical shock phenomena in homogeneous materials are also amenable to examination with this diagnostic.

A line-imaging ORVIS has been successfully interfaced to the target chamber of a compressed gas gun driver and fielded on numerous tests in combination with simultaneous measurements using a dual delay-leg, "push-pull" VISAR system. These tests include measurements of dispersive velocity in a shock-loaded explosive simulant (sugar). The dynamic response (in the absence of chemical reaction) of low-density pressings of sugar has been investigated as a function of both impact velocity and selected changes in particle size distribution. Preliminary experiments on HMX have begun to address mesoscopic scale effects arising from chemical energy release. Systematic effects observed in the wave profiles of these and other heterogeneous materials can be used to test and refine parameters and models used in corresponding 3-D numerical simulations.

To realize fully the potential of line-imaging ORVIS in this research area, it is vital to acquire a more comprehensive data base on explosives and surrogate materials. Also, it is important to establish meaningful statistical comparisons with numerical simulations that address mesoscopic scale effects. To achieve these goals, tests on low-density explosives and inert surrogates will have to be performed in multiple lots per impact condition to ensure adequate statistics and repeatability. Results should then be extensively examined in tandem with the corresponding 3-D computations using optimized methods of data reduction and statistical analysis (e.g., wavelet theory). With increased insight deriving from these efforts, it should be possible to refine and optimize inputs to the 3-D codes, as needed. Additional understanding may come from tests on other experimental systems, including samples with complex (e.g., bimodal) particle size distributions and composites containing polymeric materials or metals. Finally, there is also much room for enhancement in the mechanical and optical design of the diagnostic itself, including improvements in sample surface preparation, interferometer window coatings, and detector sensitivity.

REFERENCES

1. Baer, M. R., "Computational Modeling of Heterogeneous Reactive Materials at the Mesoscale," in *Shock Compression of Condensed Matter—1999*, edited by M. D. Furnish, et al., AIP Conference Proceedings 505, Melville, NY, 2000, pp. 27-33.
2. Gidon, S., and Behar, G. *Applied Optics* **25**, 1429-1433 (1986).
3. Mathews, A. R., Warnes, R. H., Hemsing, W. F., and Whittemore, G. R., "Line-Imaging Fabry-Perot Interferometer," in *SPIE Proc. No. 1346*, San Diego, CA, 1990, pp. 122-132.
4. Hemsing, W. F., Mathews, A. R., Warnes, R. H., and Whittemore, G. R., "VISAR: Line-Imaging Interferometer," in *SPIE Proc. No. 1346*, San Diego, CA, 1990, pp. 133-140.
5. Mathews, A. R., Boat, R. M., Hemsing, W. F., Warnes, R. H., and Whittemore, G. R., "Full-field Fabry-Perot Interferometer," in *Shock Compression of Condensed Matter—1991*, edited by S. C. Schmidt, et al. New York, Elsevier, 1992, pp. 759-762.

6. Barker, L. M., “Multi-Beam VISARs for Simultaneous Velocity vs. Time Measurements,” in *Shock Compression of Condensed Matter—1999*, edited by M. D. Furnish, et al., AIP Conference Proceedings 505, Melville, NY, 2000, pp. 999-1002.
7. Baumung, K., Singer, J., Razorenov, S. V., and Utkin, A. V., “Hydrodynamic Proton Beam-Target Interaction Experiments Using an Improved Line-Imaging Velocimeter,” in *Shock Compression of Condensed Matter—1995*, edited by S. C. Schmidt and W. C. Tao, Woodbury, NY: AIP Press, 1996, pp. 1015-1018.
8. Bloomquist, D. D., and Sheffield, S. A., *J. Appl. Phys.* **54**, 1717-1722 (1983).
9. Bloomquist, D. D., and Sheffield, S. A., "ORVIS, Optically Recording Velocity Interferometer System, Theory of Operation and Data Reduction Techniques," Sandia Report, SAND82-2918, February 1983.
10. Trott, W. M., and Asay, J. R., “Investigation of Microscale Shock Phenomena Using a Line-Imaging Velocity Interferometer System,” in *Shock Compression of Condensed Matter—1997*, edited by S. C. Schmidt, et al., AIP Conference Proceedings 429, New York, 1998, pp. 837-840.
11. Trott, W. M., Knudson, M. D., Chhabildas, L. C., and Asay, J. R., “Measurements of Spatially Resolved Velocity Variations in Shock Compressed Heterogeneous Materials Using a Line-Imaging Velocity Interferometer,” in *Shock Compression of Condensed Matter—1999*, edited by M. D. Furnish, et al., AIP Conference Proceedings 505, Melville, NY, 2000, pp. 993-998.
12. Trott, W. M., Castañeda, J. N., O'Hare, J. J., Knudson, M. D., Chhabildas, L. C., Baer, M. R., and Asay, J. R., "Examination of the Mesoscopic Scale Response of Shock Compressed Heterogeneous Materials Using a Line-Imaging Velocity Interferometer," in *Proceedings, Explomet™ 2000 International Conference on Fundamental Issues and Applications of Shock-Wave and High-Strain-Rate Phenomena* (in press).
13. Hemsing, W. F., *Rev. Sci. Instrum.* **50**, 73-78 (1979).
14. Diemunsch, G., and Prenel, J. P. *Optics and Laser Technology* **19**, 141-144 (1987).
15. Trott, W. M., and Meeks, K. D., “Acceleration of Thin Foil Targets Using Fiber-Coupled Optical Pulses,” in *Shock Compression of Condensed Matter—1989*, edited by S. C. Schmidt, et al., New York: Elsevier, 1990, pp. 997-1000.
16. Trott, W. M., and Meeks, K. D., *J. Appl. Phys.* **67**, 3297-3301 (1990).
17. Fisk, G. A., Mastin, G. A., and Sheffield, S. A., *J. Appl. Phys.* **60**, 2266-2271 (1986).
18. Farge, M., *Ann. Rev. Fluid Mech.* **50**, 395-457 (1992).
19. Trott, W. M., "Investigation of the Dynamic Behavior of Laser-Driven Flyers," in *High Pressure Science and Technology--1993*, edited by S. C. Schmidt, et al., New York: AIP Press, 1994, pp. 1655-1658.
20. Wise, J. L., and Chhabildas, L. C., “Laser Interferometer Measurements of Refractive Index in Shock Compressed Materials,” in *Shock Waves in Condensed Matter—1985*, edited by Y. M. Gupta, New York: Plenum Press, 1986, pp. 441-454.
21. Sheffield, S. A., Gustavsen, R. L., and Alcon, R. R., “Porous HMX Initiation Studies—Sugar as an Inert Simulant,” in *Shock Compression of Condensed Matter—1997*, edited by S. C. Schmidt, et al., AIP Conference Proceedings 429, New York, 1998, pp. 575-578.
22. Sheffield, S. A., Gustavsen, R. L., and Anderson, M. U., "Shock Loading of Porous High Explosives," in High-Pressure Shock Compression of Solids IV, edited by L. Davison, et al., New York: Springer-Verlag, 1997, pp. 23-61.
23. Thissell, W. R., Zurek, A. K., Tonks, D. L., and Hixson, R. S., "Experimental Quantitative Damage Measurements and Void Growth Model Predictions in the Spallation of Tantalum," in *Shock Compression of Condensed Matter—1999*, edited by M. D. Furnish, et al., AIP Conference Proceedings 505, Melville, NY, 2000, pp. 451-454.
24. Baer, M. R., unpublished results.

APPENDIX

Required Reportable Information
Laboratory Directed Research and Development

FY98-FY00 LDRD Project: Dispersive Measurements of Velocity in Heterogeneous Materials

Publications and Presentations:

Trott, W. M., Knudson, M. D., Chhabildas, L. C., and Asay, J. R., “Measurements of Spatially Resolved Velocity Variations in Shock Compressed Heterogeneous Materials Using a Line-Imaging Velocity Interferometer,” in *Shock Compression of Condensed Matter—1999*, edited by M. D. Furnish, et al., AIP Conference Proceedings 505, Melville, NY, 2000, pp. 993-998 (invited).

Trott, W. M., Castañeda, J. N., Knudson, M. D., Chhabildas, L. C., and Asay, J. R., "Probing Shocked Microstructures," in *Proceedings, 50th Meeting of the Aeroballistic Range Association*, Pleasanton, CA, November 8-12, 1999.

Trott, W. M., Castañeda, J. N., O'Hare, J. J., Knudson, M. D., Chhabildas, L. C., Baer, M. R., and Asay, J. R., "Examination of the Mesoscopic Scale Response of Shock Compressed Heterogeneous Materials Using a Line-Imaging Velocity Interferometer," in *Proceedings, Explomet™ 2000 International Conference on Fundamental Issues and Applications of Shock-Wave and High-Strain-Rate Phenomena* (in press).

Knudson, M. D., Bailey, J. E., Asay, J. R., Anderson, G. M., Castañeda, J. N., Bernard, M. A., Carlson, A. L., Chandler, G. A., Hall, C. A., Hanson, D. L., Johnston, R. R., Lake, P. W., Trott, W. M., and Ng, A., "Line-Imaging VISAR and Optical Spectroscopy Measurements of Shock Waves Driven in Intense Z-Pinch Radiation *AIRAPT-17 International Conference on High Pressure Science and Technology,* Honolulu, HI, July 25-30, 1999.

Trott, W. M., "Probing Energetic Materials Chemistry at the Mesoscale Using Line-Imaging Velocity Interferometry," *Gordon Research Conference on Energetic Materials*, Tilton, NH, July 2-7, 2000 (invited).

Invention Disclosures: none

Patents: none

Copyrights: none

Employee recruitment: one member of Technical Staff

Student involvement: none

Distribution:

1 Los Alamos National Laboratory
Attn: S. A. Sheffield, DX-1
P. O. Box 1663
Los Alamos, NM 87545

1	MS 0188	C. E. Meyers, 1030
1	0511	J. C. Cummings, Jr., 1010
1	0555	M. S. Garrett, 9122
1	0555	B. D. Hansche, 9122
1	0557	T. J. Baca, 9125
1	0825	W. H. Rutledge, 9115
1	0828	J. Moya, 9132
1	0828	M. Pilch, 9133
1	0834	A. C. Ratzel, 9110
1	0834	J. Johannes, 9114
5	0834	J. N. Castañeda, 9112
15	0834	W. M. Trott, 9112
1	0835	S. N. Kempka, 9111
1	0835	J. S. Peery, 9121
5	0836	M. R. Baer, 9100
1	0836	W. Hermina, 9113
1	0836	E. Hertel, 9116
1	0836	R. O. Griffith, 9117
1	0841	T. C. Bickel, 9100

Distribution (cont.):

1	0847	H. S. Morgan, 9120
1	0847	D. R. Martinez, 9124
1	0847	R. A. May, 9126
1	1135	D. B. Davis, 9134
1	1168	M. D. Furnish, 1612
5	1181	J. R. Asay, 1610
5	1181	L. C. Chhabildas, 1610
5	1181	J.-P. Davis, 1610
1	1181	C. A. Hall, 1610
5	1181	M. D. Knudson, 1610
1	1181	W. D. Reinhart, 1610
1	1181	T. F. Thornhill III, 1610
1	1186	R. J. Lawrence, 1674
1	1421	R. E. Setchell, 1122
1	1421	M. U. Anderson, 1122
1	1454	L. L. Bonzon, 2554
1	1454	A. M. Renlund, 2554
1	9018	Central Technical Files, 8940-2
2	0899	Technical Library, 9616
1	0612	Review & Approval Desk, 9612 For DOE/OSTI